Spontaneous imbibition in porous media: comparisons between a dynamic pore-network model and a VOF direct numerical simulation model

Chao-Zhong Qin[1], Harald van Brummelen[2], and Mahmoud Hefny[3]

[1]Eindhoven University of Technology
[2]Technology University of Eindhoven
[3]ETH Zurich

November 22, 2022

Abstract

The dynamic pore-network modeling, as an efficient pore-scale tool, has been used to understand spontaneous imbibition in porous media, which plays an important role in many subsurface applications. In this work, we aim to compare a dynamic pore-network model of spontaneous imbibition with the VOF (volume of fluid) model. The μCT scanning of a porous medium of sintered glass beads is selected as our study domain. We extract its pore network by using an open-source software of PoreSpy, and further project the extracted information of individual watersheds into multiform idealized pore elements. A number of case studies of primary spontaneous imbibition have been conducted by using both the pore-network and the VOF models under different wettability values and viscosity ratios. We compare those model predictions in terms of imbibition rates and temporal saturation profiles along the flow direction. We show that the pore-network model can reproduce the VOF model results for an air-water system, in which water is the wetting phase. For a more viscous nonwetting phase such as oil, however, the pore-network model predicts a slower imbibition process and a rougher wetting front, in comparison to the predictions by the VOF model.

Spontaneous imbibition in porous media: comparisons between a dynamic pore-network model and a VOF direct numerical simulation model

Chao-Zhong Qin[1,2,*], Harald van Brummelen[3], Mahmoud Hefny[4,5]

1. State Key Laboratory of Coal Mine Disaster Dynamics and Control, Chongqing University, Chongqing, China
2. School of Resources and Safety Engineering, Chongqing University, Chongqing, China
3. Department of Mechanical Engineering, Eindhoven University of Technology, The Netherlands
4. Geothermal Energy and Geofluids, Institute of Geophysics, ETH Zürich, Switzerland
5. Geology Department, South Valley University, Egypt

The corresponding author:

Chao-Zhong Qin

chaozhong.qin@gmail.com

State Key Laboratory of Coal Mine Disaster Dynamics and Control,

Chongqing University, Chongqing, 400044, China

Highlights

- We conduct dynamic pore-network modeling of spontaneous imbibition in a porous medium of sintered glass beads.
- We conduct extensive comparisons between the pore-network model and the VOF model under different wettability values and viscosity ratios.
- The pore-network model can reproduce the VOF model results for an air-water system in which water is the wetting phase.
- Without explicitly tracking the main terminal meniscus in a pore body, the pore-network model predicts a rougher wetting front and a slower imbibition process for a highly viscous nonwetting phase.

Abstract

The dynamic pore-network modeling, as an efficient pore-scale tool, has been used to understand spontaneous imbibition in porous media, which plays an important role in many subsurface applications. In this work, we aim to compare a dynamic pore-network model of spontaneous imbibition with the VOF (volume of fluid) model. The μCT scanning of a porous medium of sintered glass beads is selected as our study domain. We extract its pore network by using an open-source software of PoreSpy, and further project the extracted information of individual watersheds into multiform idealized pore elements. A number of case studies of primary spontaneous imbibition have been conducted by using both the pore-network and the VOF models under different wettability values and viscosity ratios. We compare those model predictions in terms of imbibition rates and temporal saturation profiles along the flow direction. We show that the pore-network model can reproduce the VOF model results for an air-water system, in which water is the wetting phase. For a more viscous nonwetting phase such as oil, however, the pore-network model predicts a slower imbibition process and a rougher wetting front, in comparison to the predictions by the VOF model.

Plain Language Summary

The flow of a fluid into porous media by capillary force is encountered in many everyday processes, such as water-flow to reach the tips of trees and water-flow through soil. These processes are examples of spontaneous imbibition. Spontaneous imbibition is also crucial to many industrial applications, ranging from oil recovery and sequestration of carbon dioxide to inkjet printing and paper sensors. Mostly the imbibition rate, the roughening of the imbibition front, and the trapping of the nonwetting phase are of interest. In this regard, pore-scale modeling of spontaneous imbibition in porous media is indispensable, given the fact that experiments are costly and restricted by data access to the inside of media. Here we present a dynamic pore-network model of spontaneous imbibition, which is much more computationally efficient than direct numerical simulations (e.g., the VOF model). This allows to model a large porous medium for the upscaling study, which is usually prohibitive to direct numerical simulations. We conduct extensive comparisons between the pore-network model and the VOF model. We show that the pore-network model can reproduce the VOF model results for an air-water system, in which water is the wetting phase.

1. Introduction

Spontaneous imbibition plays an important role in many subsurface applications such as oil recovery in fractured reservoirs (Liu et al., 2020; Morrow and Mason, 2001) and geological sequestration of carbon dioxide (Guo et al., 2016). In those applications, the imbibition rate and the trapping of nonwetting phase are of great interest. Spontaneous imbibition is usually categorized into cocurrent and countercurrent spontaneous imbibition. In cocurrent spontaneous imbibition, the wetting phase enters a porous medium through one boundary, while the nonwetting phase is displaced from the medium via other boundaries. By contrast, in countercurrent spontaneous imbibition, the wetting and nonwetting phases respectively enter and leave a porous medium at the same boundary. In this work, we focus on cocurrent spontaneous imbibition. Henceforth, spontaneous imbibition is referred to as cocurrent spontaneous imbibition, unless otherwise stated.

To predict the imbibition rate by the two-phase Darcy model, a number of material properties need to be determined such as capillary pressure and relative permeability (Alyafei et al., 2016; Schmid et al., 2016). Moreover, sharp wetting fronts observed in many core-scale experiments (Akin et al., 2000; Alyafei et al., 2016; Kuijpers et al., 2017) indicate that *dynamics* in spontaneous imbibition is strong, particularly at its early stage. This challenges conventional measurements of material properties which were mostly conducted in equilibrium or steady state (Zhuang et al., 2017). In this regard, pore-scale models of spontaneous imbibition are invaluable to explore the dynamic effect on those material properties. Furthermore, it helps to improve Darcy-scale imbibition models.

There have been extensive pore-scale numerical studies of two-phase flow in porous media, which cover a wide spectrum of research interests (Joekar-Niasar et al., 2010; Kunz et al., 2016; Qin, 2015; Raeini et al., 2014; Sweijen et al., 2016). In general, pore-scale models can be classified into first-principle models based on the Navier-Stokes equation, and pore-network models. First-principle models in porous media research are also called DNS (Direct Numerical Simulation) models. Popular DNS models include VOF (Volume of Fluid) model, LBM (Lattice-Boltzmann method), SPH (Smoothed Particle Hydrodynamics), and phase-field models (Shokrpour Roudbari et al., 2016; Yue and Feng, 2011). Although DNS models resolve complex porous structures directly, they are restricted by severe computational efforts. In addition, favorable contact angle values have been often used in simulations due to the deficiency of embedded contact line dynamics in DNS models. Later on, we will show this deficiency in our VOF simulations of spontaneous imbibition. Alternatively, pore-network models first discretize complex pore structures into connected pore elements. Then, in conjunction with local rules, mass conversation of each phase is solved with the

help of element-scale constitutive relations. In such way, pore-network models not only reduce computational efforts considerably, but also represent the pore-structure information adequately (Aghaei & Piri, 2015; Qin & van Brummelen, 2019). If dynamic effects can be neglected, pore-network models reduce to be quasi-static. Quasi-static pore-network models have been widely used in obtaining material properties such as relative permeability and capillary pressure (Patzek, 2001; Raeini et al., 2019). They have been widely used in the study of CO_2 trapping in the geological carbon storage (Valvatne and Blunt, 2004).

Up to now, dynamic pore-network models have been mostly used to qualitatively investigate fundamentals of two-phase flow in porous media (Huang et al., 2016; Joekar-Niasar et al., 2010; Li et al., 2017; Médici and Allen, 2013; Qin et al., 2019; Qin, 2015; Sheng and Thompson, 2016). Although a few imbibition models (Aghaei and Piri, 2015; Hughes and Blunt, 2000; Li et al., 2017; Nguyen et al., 2006; Sun et al., 2016; Tørå et al., 2012; Wang et al., 2015) under the constant-flux condition have been reported, either the used pore networks did not represent complex pore structures or the used local rules are not adequate to spontaneous imbibition. Verification studies of the dynamic pore-network modeling are scant in the open literature, because (1) experimental data with high temporal resolution is difficult to obtain, and (2) oversimplified pore elements cannot well represent realistic pore structures. Recently, a comparison of the dynamic pore-network modeling of primary drainage against micromodel experiments has been reported under constant-flux boundary conditions (Yang et al., 2017). The authors showed that at breakthrough, the distribution of the nonwetting phase saturation along the flow direction matches experimental data well. However, for spontaneous imbibition, both imbibition rates and saturation profiles are of interest, and a pressure boundary condition is relevant. In principle, pore-scale events in imbibition processes are more complicated than those in drainage processes. Thus, a pore-network model for spontaneous imbibition requires specifically-defined local rules such as the competition of arc menisci (AMs) filling and main terminal meniscus (MTM) movement (Mason and Morrow, 1991).

To address the above-mentioned challenges, we have developed a dynamic pore-network model for spontaneous imbibition in porous media (Qin and van Brummelen, 2019). Multiform idealized pore elements have been used to represent complex pore structures so that our model bears the potential to quantitatively predict spontaneous imbibition for a ‘real’ porous medium. Preliminary case studies show that our model captures essentials of spontaneous imbibition such as imbibition rates and sharp wetting fronts (Gruener et al., 2012). In this work, we extend the dynamic pore-network model into spontaneous imbibition in ‘real’ granular porous media. We aim to compare our pore-network model with the VOF model in terms of imbibition rates and temporal saturation

profiles under different wettability values and viscosity ratios. In addition, we address the impact of voxel-induced roughness on the prediction of VOF simulations for digital porous media such as those obtained by μCT. To this end, we use a small piece of μCT scanning of sintered glass beads (Hoang et al., 2018), which resembles highly-permeable sandstones or carbonate rocks. In this work, we focus on the early stage of spontaneous imbibition in porous media where dynamics is strongest. PoreSpy (Gostick, 2017) is used to extract the pore-network information, which is properly projected into well-defined idealized pore elements. It is worth noting that the verification of VOF simulations or the pore-network modeling of spontaneous imbibition against experiments is excluded in this work, because benchmark data of spontaneous imbibition for the verification of pore-scale models are still absent in the open literature, to the best of our knowledge.

The remainder of the paper is structured as follows. In section 2, we introduce the dynamic pore-network model. In section 3, we present the used VOF model, which is implemented in the commercial solver FLUENT. The comparison of pore-network modeling results and VOF results is given and discussed in section 4, which is followed by the main conclusions in section 5.

2. Pore-network model

Our dynamic pore-network model comprises three elements: (1) a pore network representing the topology and the morphology of porous structures, (2) governing equations of mass conservation, and (3) constitutive relations assisted by local rules. The details of the pore-network model can be found in (Qin and van Brummelen, 2019). In this section, we briefly present the governing equations and key local rules. We focus on the pore-network extraction via PoreSpy (Gostick, 2017), and the preparation of the pore network to be used in the modeling.

2.1 Pore-network extraction

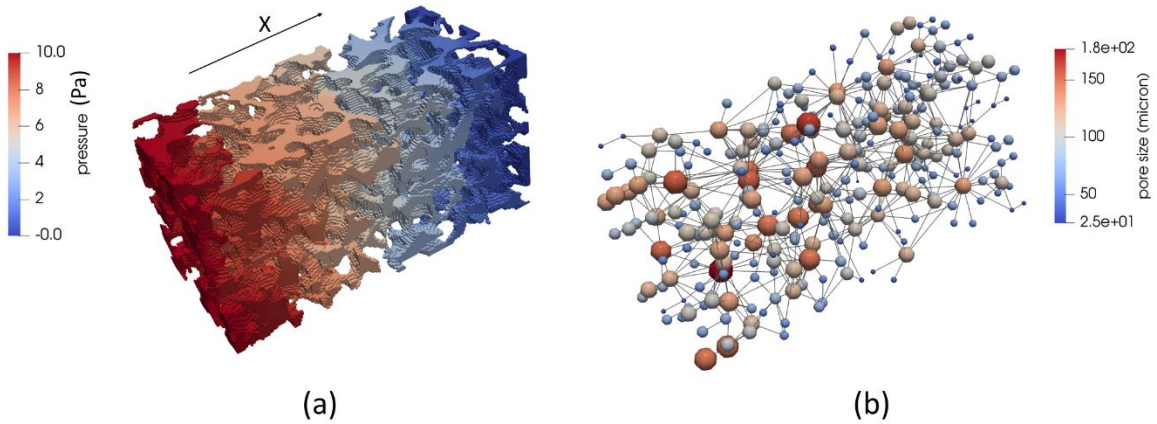

Fig. 1: (a) Pore voxels of the µCT scanning of sintered glass beads. The color map shows the single-phase pressure. (b) The corresponding pore network extracted by the open source software of PoreSpy. The color map shows the pore-body size (i.e., the inscribed radii of pore bodies).

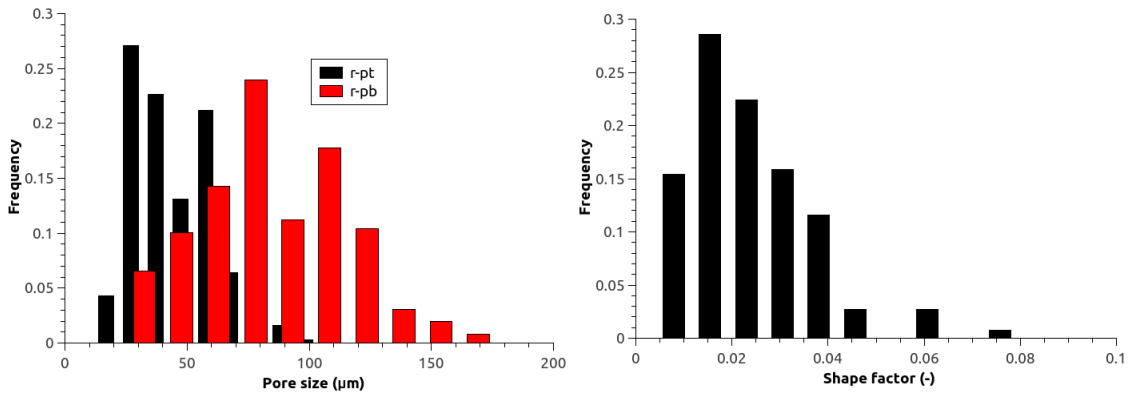

Fig. 2: (Left) pore-body and pore-throat size distributions, and (right) the shape factor distribution of pore bodies.

An open-source extraction code, PoreSpy, has been used to obtain the pore-network connectivity and geometric information of individual pores (Gostick, 2017). Watershed segmentation is used in the construction of pore bodies, while pore throats connecting pore bodies are volumeless (Rabbani et al., 2016). The key steps in the PoreSpy algorithm include (1) peak identification in the distance map, (2) removal of peaks on saddles and peaks which are too close to each other, and (3) watershed segmentation of pore spaces into pore bodies.

By PoreSpy we obtain the following pore-network information: (1) the connectivity map, (2) pore-body locations, inscribed and extended radii, and surface areas, and (3) pore-throat locations, inscribed and extended radii, perimeters, and cross-sectional areas. We project those information into idealized pore elements used in the dynamic pore-network model as follows. First, the inscribed radius in a pore body is equal to the inscribed radius of the corresponding watershed as $r_{pnm} = r_{ct}$, where the subscripts pnm and ct refer to the pore network and the original CT data respectively. Second, the pore-body length is approximated as $r_{ct} + R_{ct}$ where R_{ct} denotes the extended radius. Third, by virtue of volume conservation, the cross-sectional area of the pore body can be calculated as:

$$A_{pnm} = \frac{V_{ct}}{r_{ct}+R_{ct}} \tag{1}$$

where V_{ct} is the watershed volume. Fourth, together with r_{pnm}, the cross-sectional perimeter is given as (Patzek and Kristensen, 2001):

$$P_{pnm} = \frac{2V_{ct}}{r_{ct}(r_{ct}+R_{ct})} \tag{2}$$

Finally, the shape factor of the pore body is calculated according to $G_{pnm} = A_{pnm}/P_{pnm}^2$. Once the shape factor is known, an idealized pore body can be generated (Qin and van Brummelen, 2019). We notice that surface areas cannot be directly projected due to the limitation of idealized pore bodies. Although they would determine the flow resistance between neighbouring pore bodies, in this work we calibrate pore-throat sizes to match the intrinsic permeability. In our pore-network model for spontaneous imbibition, a volumeless pore throat is mainly used to account for the flow resistance of the two connected pore bodies. Therefore, we did not use the extracted cross-sectional information of pore throats, but numerically generated the pore-throat sizes by calibrating the intrinsic permeability. The shape factor of a pore throat is approximated as $G_{ij} = 0.5\left(G_i + G_j\right)$ where the subscripts i and j denote the pair of pore bodies.

The μCT image of sintered glass beads in the case studies has 200, 100, and 100 voxels along the X, Y, and Z directions, respectively. The voxel resolution is 25 μm. After segmentation, the pore voxels are shown in Fig. 1a. Fig. 1b shows the extracted pore network by PoreSpy, which has 302 pore bodies and 670 pore throats. In detail, there are 250 pore bodies with triangular cross-sections, 27 pore bodies with square cross-sections, and 25 pores bodies with circular cross-sections. Also, there are 655, 6, and 9 pore throats with triangular, square, and circular cross-sections, respectively. The inscribed radius of a pore throat is determined by:

$$r_{ij} = [\gamma + a(0.7 - \gamma)]\min(r_i, r_j) \tag{3}$$

where a is a random value between 0 and 1, and γ is the ratio of pore throat to pore body which has the value of 0.55 in this work. The calculated pore-network permeability along the X direction is 5.9 Darcy which matches the DNS result well. We also tried other formulations (Joekar-Niasar et al., 2010; Qin and Hassanizadeh, 2015) for the pore-throat size or used pore-throat sizes given by PoreSpy. Only minor differences were seen in the imbibition results. We notice that different approximations of pore-throat conductance have been used in different extraction algorithms (Yi et al., 2017). An improved method of determining the flow resistance of a pore throat would rely on the analysis of media axis and media planes along its connected pore bodies. Alternatively, one may obtain the single-phase conductance of each pore throat directly from direct numerical simulations (Zhao et al., 2020). This will be explored in a further study. The details of the μCT data and the pore-network information are given in Table 1.

2.2 Governing equations

By virtue of the incompressibility assumption, conservation of mass of the two phases translates into conservation of volume. The volumetric conservation of each phase is given as:

$$V_i \frac{ds_i^\alpha}{dt} - \sum_{j=1}^{N_i} K_{ij}^\alpha \left(p_i^\alpha - p_j^\alpha\right) \qquad \alpha = \{n, w\} \tag{4}$$

where i is the pore-body index, ij is the pore-throat index, n and w indicate the nonwetting and wetting phases, respectively, N_i is the coordination number of pore body i, V [m^3] is the volume, s [-] is the saturation, K [m^3/Pa/s] is the conductivity, and p [Pa] is the pressure. The gravity is neglected.

With the definition of mixture pressure, $\bar{p} = p^n s^n + p^w s^w$, and adding the two conservation equations together (Eq.1 for the wetting phase and for the nonwetting phase), the pressure equation is derived as (Joekar-Niasar et al., 2010):

$$\sum_{j=1}^{N_i}\left(K_{ij}^n + K_{ij}^w\right)\left(\bar{p}_i - \bar{p}_j\right) = -\sum_{j=1}^{N_i}\left\{\left[K_{ij}^n s_i^w - K_{ij}^w(1 - s_i^w)\right]p_i^c + \left[K_{ij}^w\left(1 - s_j^w\right) - K_{ij}^n s_j^w\right]p_j^c\right\} \quad (5)$$

where the capillary pressure in pore body i is defined as $p^c = p^n - p^w$.

2.3 local rules

Here, we briefly describe the main local rules used in the pore-network model. Their numerical implementations and sensitivity studies can be found in (Qin & van Brummelen, 2019). First, the imbibition pore-network model incorporates the competition between arc menisci (AMs) filling at corners and main terminal meniscus (MTM) filling (Mason and Morrow, 1991). We found that in the early stage of spontaneous imbibition the MTM filling is dominant. Second, while the MTM filling is active, empirically we assume the nonwetting phase in a pore body is trapped once either of the following two conditions is satisfied: (1) the wetting saturation in the pore body is larger than 0.9, and (2) all pore throats connected to the pore body block the nonwetting-phase transport. A small amount of nonwetting phase in the pore body may be trapped under the MTM filling. The value of 0.9 here is empirically selected in order to (1) make this value close to 1 corresponding to a fully saturated pore body, and (2) match the wetting saturation behind the wetting front which may be obtained by experiments. Once the nonwetting phase in a pore body is trapped, the nonwetting conductance of all connected pore throats is zero. While the AMs filling is active, the wetting-phase trapping is determined by snap-off conditions of its connected pore throats. Third, when the wetting saturation in a pore body reaches the value of 0.9, a transition function of the wetting saturation is used to force the capillary pressure to fast approach zero.

The main features of the present pore-network model for spontaneous imbibition include: (1) depending on flow conditions, the wetting-phase filling of a pore body can be automatically switched between the AMs filling and the MTM movement; (2) trapping of the nonwetting phase because of heterogeneous pore structures is implemented; (3) multiform pore elements are used in the model development, which allows to simulate spontaneous imbibition in a ‘real’ porous medium. The governing equations (4, 5) are numerically solved for the primary variables: wetting saturation, s_i^w, and mixture pressure, $\bar{p}_i$. At the end of each time step, the remaining quantities such as capillary pressure and phase conductivity are updated based on the primary variables. The details of the calculation of constitutive relations are presented in (Qin & van Brummelen, 2019). For all case studies in this work, the mass imbalance of the wetting phase is negligible, see Appendix B for details.

3. VOF (volume of fluid) model

We use the VOF model to explicitly track interfaces between the nonwetting and wetting phases. Both phases are incompressible, and the flow is isothermal. In the VOF model, each computational cell is either one-phase or two-phase occupied. The phase fraction is defined as:

$$a^{\alpha} = \frac{V^{\alpha}}{V_{cell}} \qquad \alpha = \{n,\ w\} \tag{6}$$

where α [-] is the phase indicator, V^{α}[m^3] is the volume of phase α in the computational cell, and V_{cell} is the volume of the computational cell. The governing equations of fluid flow in the VOF model are given as:

$$\nabla \cdot \mathbf{v} = 0 \tag{7}$$

$$\frac{\partial(\rho \mathbf{v})}{\partial t} + \nabla \cdot (\rho \mathbf{v}\mathbf{v}) = -\nabla p + \mu \nabla^2 \mathbf{v} + \mathbf{F} \tag{8}$$

$$\frac{\partial a^w}{\partial t} + \nabla \cdot (a^w \mathbf{v}) = 0 \tag{9}$$

Here, ρ [kg/m^3] and μ [Pa s] are the mixture density and viscosity, respectively, which are defined as:

$$\rho = a^w \rho^w + (1 - a^w)\rho^n \tag{10}$$

$$\mu = a^w \mu^w + (1 - a^w)\mu^n \tag{11}$$

In Eq. 8, the source term, **F** [Pa/m], due to the addition of surface tension, is calculated by the continuum surface force (CSF) model (Brackbill et al., 1992) as:

$$\mathbf{F} = \sigma \frac{2\rho k \nabla a^w}{\rho^w + \rho^n} \tag{12}$$

where σ is the surface tension (N/m), and k [1/m] is the curvature of the nonwetting-wetting interface calculated by $\nabla \cdot (\nabla a^w / |\nabla a^w|)$.

To consider the wall adhesion, the meniscus normal in a two-phase occupied computational cell next to the wall is given as:

$$\mathbf{n} = \mathbf{n}^s \cos\theta + \mathbf{t}^s \sin\theta \tag{13}$$

where $\mathbf{n}^s$ and $\mathbf{t}^s$ are the unit vectors normal and tangential to the wall, respectively, and θ is the static contact angle.

The commercial solver FLUENT 17.2, which is (Finite Volume Method) FVM-based, is used to solve the governing equations (7-9). The SIMPLE scheme is used to solve the Navier-Stokes equations (7, 9). The second-order upwind scheme is used for the momentum discretization. Eq. 9 describes the transport of the volume fraction of wetting phase, which is a hyperbolic partial differential equation. Its discretization is crucial to VOF simulations. In this work, we use the

geometric reconstruction scheme, which represents the nonwetting-wetting interface in a computational cell by a piecewise-linear approach (FLUENT 17.2 User's Guide).

For transient VOF simulations, the time step is crucial to numerical accuracy and computational cost. A large time step would give rise to smeared interfaces and even unreliable results, while a small time step entails huge computational efforts. To balance the two effects, we choose time steps such that the global Courant number is less than 0.5. For all simulated cases, in each time step, either the scaled residuals of all the equations are less than 10^{-6} or the maximum iteration number is over 50. The results show that before breakthrough of the wetting phase, the residual of 10^{-6} can be always reached.

The pore voxels of the µCT scanning as seen in Fig. 1a have been used as the computational cells in the VOF simulations. Since the mean pore size in radius is around 95 µm, this means that we have at least 8×8 cells of an average flow cross-section. Furthermore, the effect of mesh density on predicted imbibition rates will be explored in the study of simple capillary tubes in section 4.

Table 1: Geometrical and physical parameters used in the case studies.

µCT data	
Number of voxels in X, Y, and Z directions	200×100×100
Voxel resolution	25 µm
Porosity	0.27
Permeability	6.0×10^{-11} m^2
Pore network information	
Number of pore bodies and pore throats	302/670
Number of inlet and outlet pores	18/25
Porosity	0.27
Permeability	5.9×10^{-11} m^2
Mean pore size	95.2 µm
Physical parameters and model settings	
Water/air density	1000/1.2 kg/m^3
Water/air viscosity	$1.0\times10^{-3}/1.79\times10^{-5}$ Pa s
Surface tension	0.073 N/m
Inlet/outlet pressure	0.0/0.0 Pa

4. Test cases of spontaneous imbibition by the VOF model

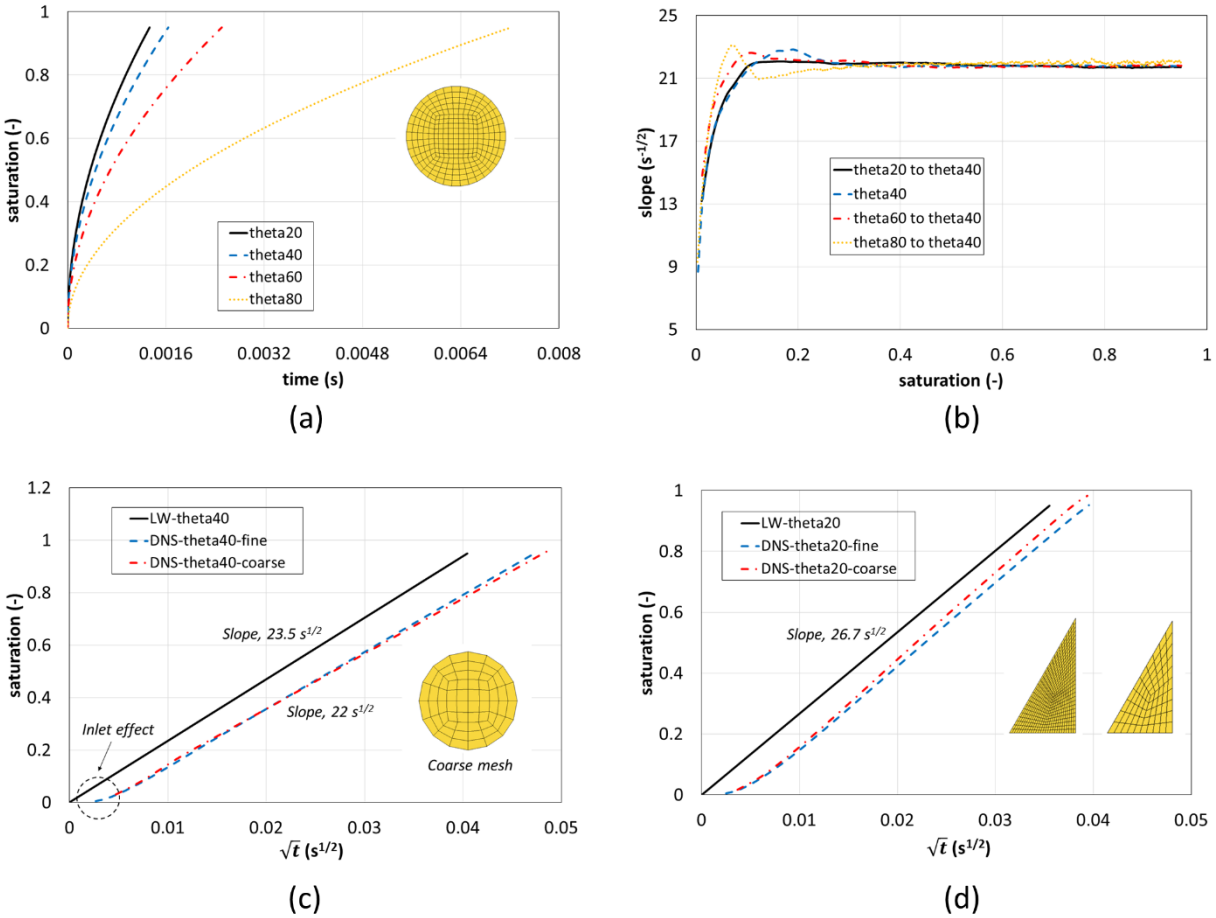

Fig. 3: Numerical studies of spontaneous imbibition of water into dry capillary tubes by the VOF model for the physical parameters and model settings in Table 1. (a) Spontaneous imbibition in a capillary tube of circular cross-section under different contact angle values. The radius of the cross-section is 20 µm, the tube length is 1 mm, and the inset shows the cross-sectional mesh, which is termed as 'fine mesh'. (b) The imbibition slope values versus saturation scaled by $\sqrt{\cos 40^{\circ} / \cos\theta}$. (c) Comparison of the imbibition rates predicted by the Lucas-Washburn (LW) equation and the VOF model under the contact angle of 40°. The inset shows the coarse cross-sectional mesh. (d) Comparison of the imbibition rates predicted by the LW equation and the VOF model under the contact angle of 20° in a capillary tube of right triangular (one corner of 30°) cross-section. The inscribed radius is 20 µm, the tube length is 1 mm, and the inset shows the fine and coarse cross-sectional meshes.

In this section, we conduct case studies of spontaneous imbibition in simple capillary tubes, in order to understand the impact of mesh-density and mesh-type (i.e., conforming mesh and voxel mesh) on the predicted imbibition rate by the VOF model. Fig. 3a shows the tube-scale saturation versus the imbibition time under four different contact angle values in a capillary tube of circular cross-section. The inset shows the used 'fine mesh'. This mesh has 19 elements along the diagonal and 36 elements along the circumference. Fig. 3b shows the corresponding scaled imbibition slope values versus saturation. The imbibition slope is defined as $S/\sqrt{t}$, in which S is the tube-scale water saturation and

t is the imbibition time. For each contact angle value θ, the scaling is $\sqrt{\cos 40^{\circ} / \cos\theta}$. It is seen that all curves collapse into the master curve of the contact angle value of 40°, except for some initial fluctuations due to the so-called inlet effect in DNS simulations (Yin et al., 2019). In Fig. 3c, we decrease the mesh-density by 2, and compare the predicted imbibition rates, which are also compared with that by the LW equation (i.e., $S = \sqrt{r\sigma\cos\theta/(2\mu L^2)}$, in which r is the radius, σ is the surface tension, μ is the water dynamic viscosity, and L is the tube length). The differences in the imbibition rates predicted by the VOF model with a fine mesh and a coarse mesh are negligible. In addition, the imbibition rates predicted by the VOF model match with that of the LW equation. For spontaneous imbibition in a capillary tube of triangular cross-section, as shown in Fig. 3d, the predicted imbibition rate of the coarse mesh is slightly larger than that under the fine mesh. However, both results match well with that of the LW equation. Notice that in the calculation of imbibition rate by the LW equation for the capillary tube of right triangular cross-section, the entry pressure (i.e., the capillary pressure) is calculated by the MS-P theory (Mayer and Stowe, 1965; Princen, 1970).

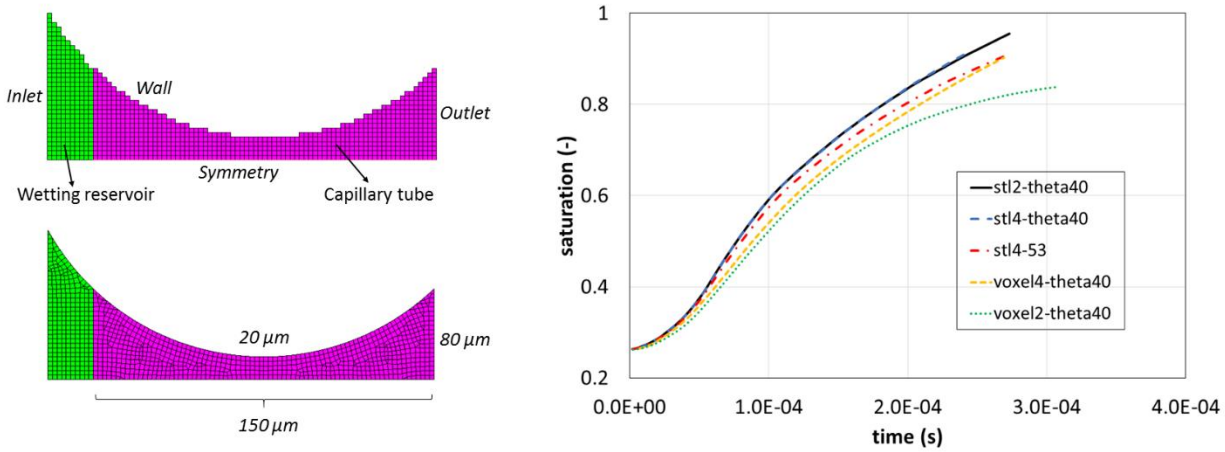

Fig. 4: (Left) Voxel representation and smooth representation (i.e., STL) of a 2D capillary tube and their associated computational meshes. (Right) Imbibition rates under two different meshing methods. The notation of '*stl4-theta40*' in the legend denotes the case study of the smooth-geometry representation with the contact angle of 40°. The mean element size is around 4 µm. The notation of '*voxel2-theta40*' in the legend indicates the case study of the voxel-representation with the contact angle of 40°. The voxel size is 2 µm.

We further study the impact of mesh-type and mesh-refinement on the imbibition rate for a single 2D curved capillary tube. The left graph in Fig. 4 shows the voxel-representation and smooth-geometry representation of the half of a 2D capillary tube. The wall-boundary length of the voxel-representation (due to voxel-induced roughness) is longer than that of the smooth representation by 27%. The computational domain includes the wetting reservoir and the converging and diverging

tube. The radius of the tube throat and the radius of the outlet are 20 μm and 80 μm, respectively. The length of the tube is 150 μm. Initially the tube is saturated with air; then water imbibes in. The right graph of Fig. 4 shows the imbibition rates under different mesh types and mesh densities. First, it is seen that for the smooth-geometry representation the mesh size of 4 μm and 2 μm give the same imbibition rate, while for the voxel-representation reducing the mesh size of 4 μm to 2 μm gives slightly slower imbibition rate in the converging part of the tube, but much slower imbibition rate in the diverging part of the tube. We note that the refinement of the voxel-representation here is different from a higher voxel-resolution of the porous medium. The refinement here is conducted on the fixed voxel resolution of 4 μm. Second, with the same mesh density the VOF model predicts a faster imbibition process for the smooth-geometry representation than that for the voxel-representation. This is mainly due to the voxel-induced roughness of the wall, owing to the fact that a rough wall increases the dissipation energy around three-phase contact lines. To include this influence in the smooth-geometry representation, we may revise the static contact angle by (Forsberg et al., 2010):

$$\tilde{\theta} = \arccos\left(\frac{S^{stl}}{S^{voxel}}\cos\theta\right) \tag{14}$$

where θ is the contact angle used in the voxel-representation, S^{stl} denotes the wall surface area of the smooth-geometry representation (in 2D it is the wall length), S^{voxel} denotes the wall surface area of the voxel-representation. For the capillary tube under study, the revised contact angle value used for the smooth-geometry representation would be 53° for the contact angle value of 40° used for the voxel-representation. After the contact angle modification, the difference between the imbibition rate for the smooth-geometry representation and the imbibition rate for the voxel-representation is considerably reduced.

Based on the above case studies, we may conclude that the mesh density with the voxel resolution of 25 μm is adequate for our VOF simulations of spontaneous imbibition in the μCT scanning of sintered glass beads. Similar mesh densities have also been reported in VOF simulations of two-phase dynamics in porous media ((Ferrari et al., 2015; Raeini et al., 2014). Additionally, we show that the impact of voxel-induced roughness on the imbibition rate can be alleviated by using Eq. 14 to revise the static contact angle.

5. Results and discussion

A number of case studies of the primary imbibition by both pore-network model and VOF model are conducted under different contact angle values and viscosity ratios. The used physical parameters and boundary conditions are given in Table 1. We compare the prediction results of pore-network modeling and VOF simulations in term of imbibition rates and temporal saturation profiles along the flow direction. Moreover, we explore the influence of viscosity ratio on the trapping of nonwetting phase in spontaneous imbibition.

5.1 Imbibition rates

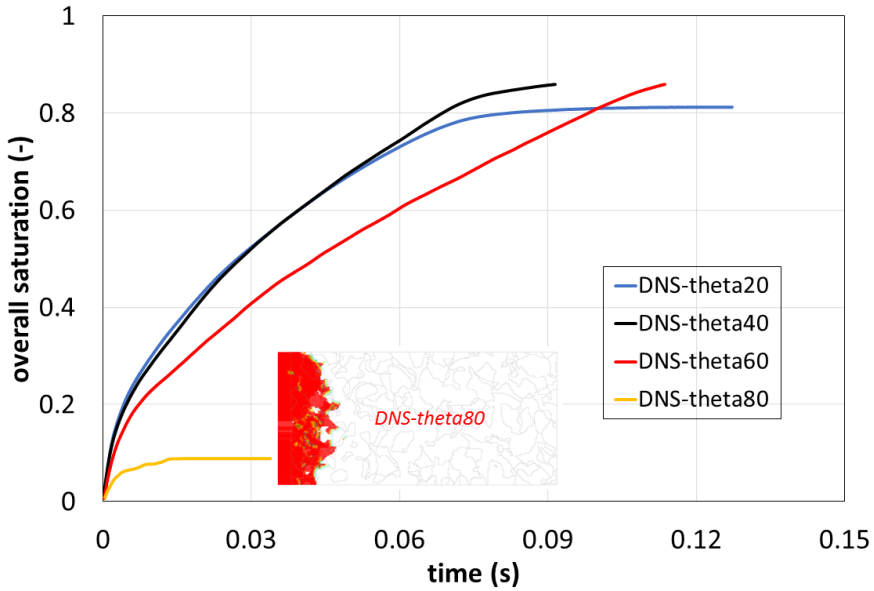

Fig. 5: Imbibition rates under four different static contact angle values predicted by the VOF model for the air-water system. The inset shows that the imbibition front stops at the inlet region under the static contact angle of 80°. The 'overall saturation' denotes the water saturation of the whole porous medium.

Fig. 5 shows the imbibition rates under four different static contact angle values predicted by the VOF model. The wetting and nonwetting phases are water and air, respectively. It is seen that the VOF model predicts two almost overlapping imbibition curves for the contact angle values of 20° and 40°. There are two possible reasons for this observation: (1) the current mesh density cannot resolve highly curving interfaces, particularly when interfaces move through converging pore spaces, and (2) voxel-induced roughness impacts the wall adhesion model used in the VOF simulations. When the contact angle is set to 80° corresponding to a weakly water-wet medium, the imbibition front ceases near the inlet region as shown by the inset in Fig. 5. This is mainly due to diverging pore

spaces which may locally flatten the nonwetting-wetting interfaces so that the imbibition driving force approaches to zero (Pavuluri et al., 2019). Furthermore, the CSF model (see Eq. 12) for calculating capillary forces may fail under extremely small capillary number values (Shams et al., 2018), which would numerically halt the wetting front movement. It is worth noting that experimental data show that the water imbibition front can continuously travel through porous materials with the static contact angle even larger than 80° (Kuijpers et al., 2017). To sum up, for our case studies, the VOF model does not work well on the strongly or weakly water-wet porous medium which is represented by pore-space voxels. Therefore, in this work, we select VOF simulations with the contact angle values of 40° and 60° (corresponding to intermediately water-wet porous media) to compare with the dynamic pore-network modeling. Furthermore, in Appendix B, we show that for all case studies in this work, the capillary number values are smaller than 10^{-3}. This indicates that the dynamic effect on the contact angle is minor. The wall roughness, however, would dominate the prediction uncertainties of spontaneous imbibition.

In light of the test case studies in Fig. 4, to compare the pore-network modeling results with the VOF simulation results, we have revised the contact angle values used in the pore-network modeling by Eq. 14. Our previous study shows that the voxel-representation of the porous medium under study increases the surface area of solid walls by around 45% in comparison to the smooth-geometry representation (Hoang et al., 2018). Fig. 6 shows the comparison of the imbibition rates predicted by the VOF model and the pore-network model, still for the air-water system. In the VOF simulations, two contact angle values of 40° and 60° are used, while the revised contact angle values of 58° and 69.8° are used in the pore-network modeling. It is seen that the two model predictions match very well. The pore-network model has the big advantage of computational efficiency. It takes less than one minute for one case study running on a single core, while the VOF model needs around one week of 16-core parallel computation. Fig. 7 shows the comparison of the slope values predicted by the VOF model and the pore-network model. The slope value is calculated by $\Delta S/\Delta(\sqrt{t})$ where S denotes the overall saturation, and $\sqrt{t}$ is the square root of the imbibition time. It is seen that the two models predict similar slope values except that the VOF model predicts peak values at the initial stage, in particular for the strongly wetting case ($\theta = 40^{\circ}$). We attribute this discrepancy to the fact that some uncertainties have been involved in the generation of inlet pores in the pore-network modeling. It is expected that the matching in Fig. 7 can be further improved with proper calibration of the conductance of the inlet pores. A further investigate is, however, beyond the scope of the current work.

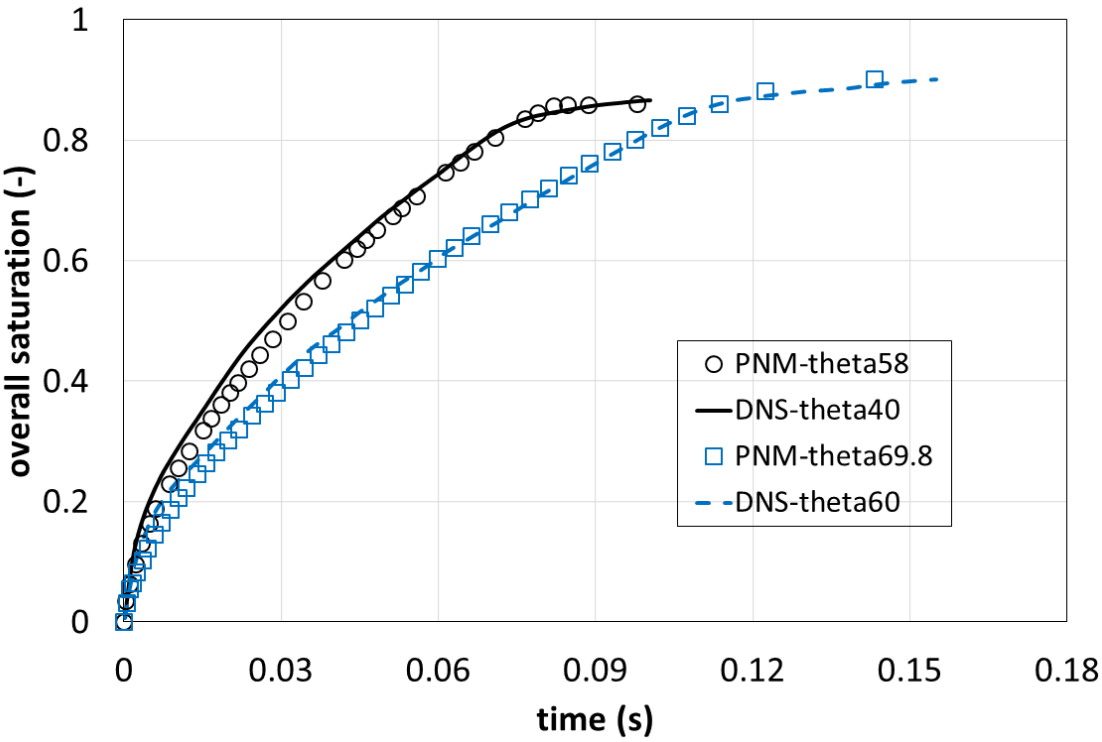

Fig. 6: Comparison of the imbibition rates predicted by the VOF model and the pore-network model for the air-water system. In the DNS simulations, two contact angle values of 40° and 60° are used, while the revised contact angle values of 58° and 69.8° are used in the pore-network modeling. The revision is done by Eq. 14.

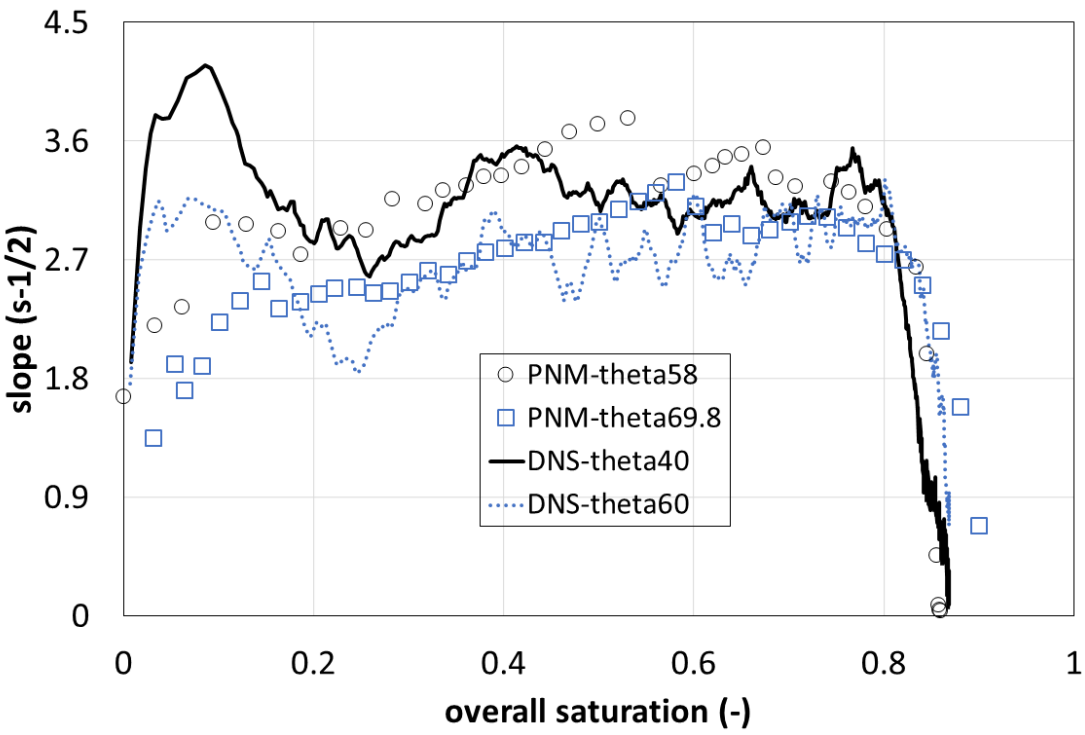

Fig. 7: Comparison of the slope values predicted by the VOF model and the pore-network model. The slope is calculated by $\Delta S/\Delta(\sqrt{t})$ where S denotes the overall saturation, and t is the imbibition time.

5.2 Phase distributions

Fig. 8 shows the water distributions in the porous medium under different overall saturation values predicted by the VOF model and the pore-network model. The nonwetting phase is air. The static contact angle used in the VOF model is 40°, while the revised contact angle used in the pore-network modeling is 58°. It is seen that the two models predict very similar water distributions. As expected, a sharp wetting front propagates in the flow direction. The imbibition is predominated by the MTM movement, with minor corner fillings observed in the wetting front.

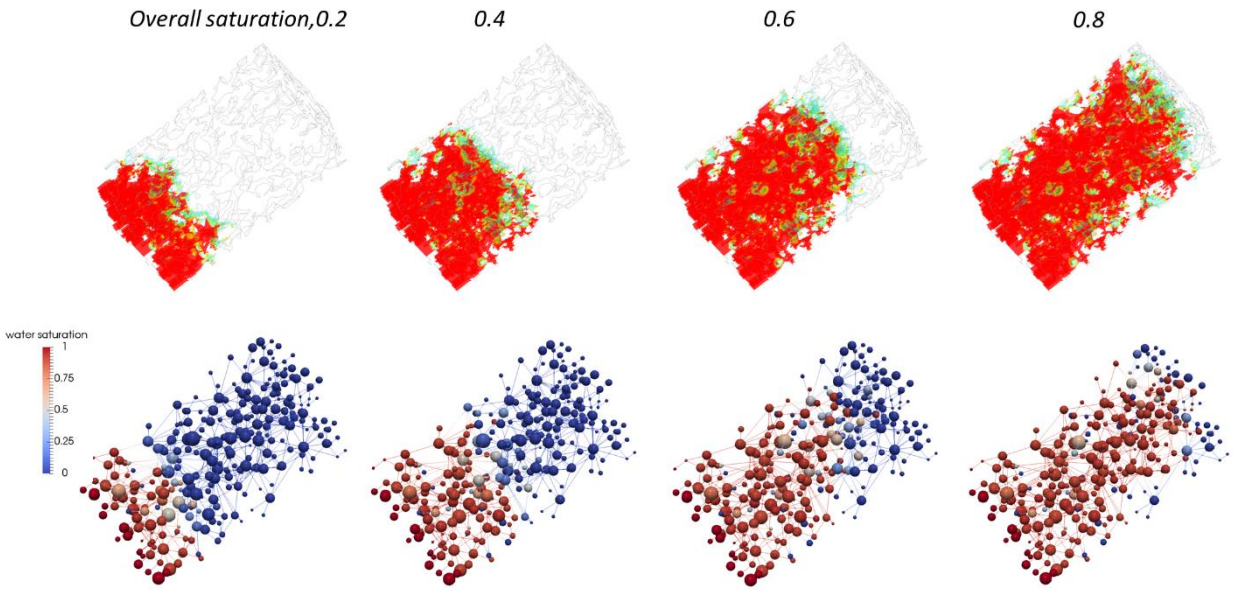

Fig. 8: Water distributions in the porous domain under different overall saturation values predicted by the VOF model (upper row) and the pore-network model. In the upper row, the red color denotes the water phase, while the empty denotes air. The static contact angle used in the VOF model is 40°.

Fig. 9 shows the corresponding distributions of water saturation profiles along the flow direction. For the pore-network modeling results, the cross-sectional saturation at each location is calculated by averaging a domain length of 500 μm, while for the VOF results, the cross-sectional saturation values are directly calculated at the same locations. It is found that the saturation profiles match each other at each overall saturation value. However, slightly more diffusive wetting fronts are observed in the pore-network modeling. This is because we do not explicitly track the movement of the MTM in a pore body in the pore-network model (Qin and van Brummelen, 2019). All connected pore throats with a pore body have equal probability to transport water into neighbouring pore bodies. As a result, the wetting front is smeared. Similar diffusive phenomena have been observed in the pore-network modeling of solute transport under high-Péclet flows (Mehmani and Tchelepi, 2017).

Nevertheless, for the air-water system, as shown in Fig. 6, our pore-network model can predict the imbibition rate well, in comparison to the VOF simulations. For the porous medium under study, Fig. 9 further shows that both models predict that a small amount of air (around 0.1 in saturation) is trapped behind the wetting front. Air is only locally trapped in pore bodies. It is worth noting that the amount of trapped nonwetting phase behind the wetting front depends on the porous structures under study. This dependence has also been seen in experimental results (Alyafei et al., 2016; Kuijpers et al., 2017).

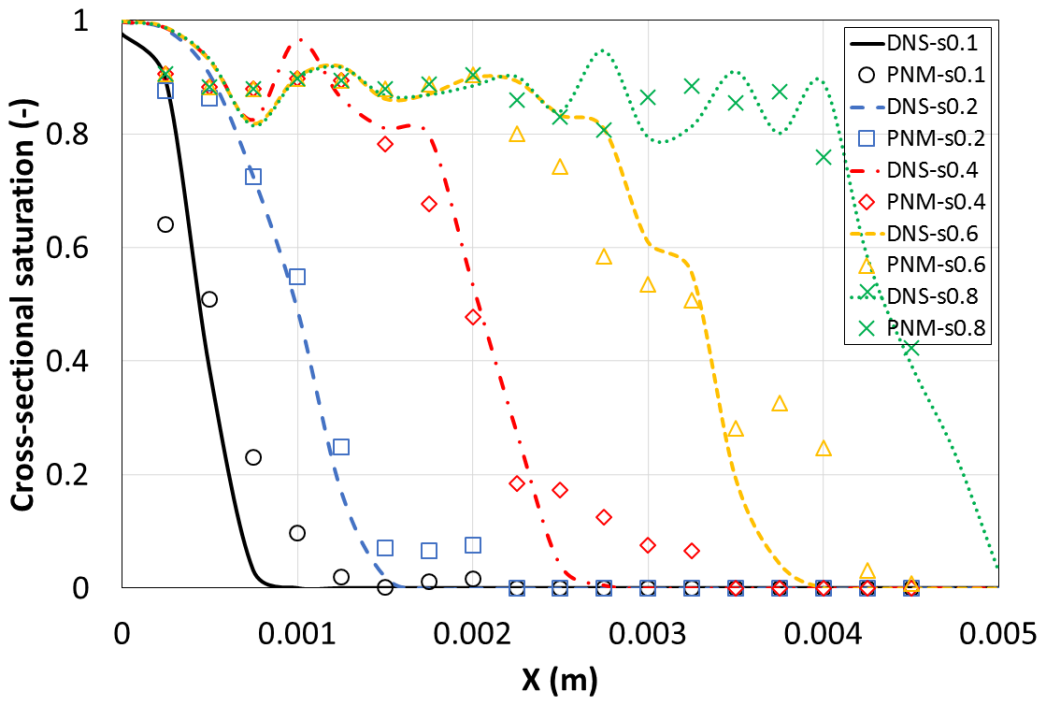

Fig. 9: Distributions of the water saturation profiles along the flow direction under different overall saturation values. For the pore-network modeling results, the cross-sectional saturation at each location is calculated by averaging a domain length of 500 µm. The static contact angle used in the VOF model is 40°.

5.3 Nonwetting-phase viscosity effect on the imbibition

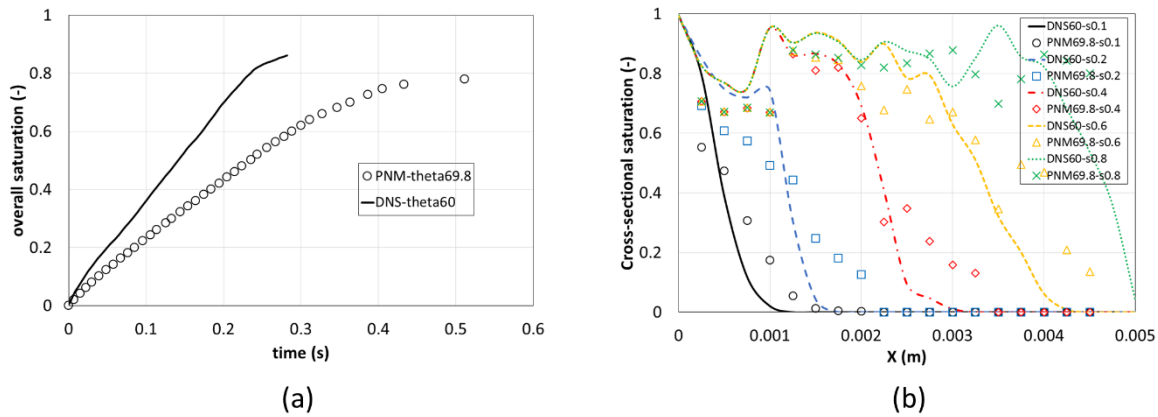

Fig. 10: (a) Comparison of the imbibition rates predicted by the VOF model and the pore-network model for the oil-water system. The oil viscosity is 1.0×10^{-3} Pa s. (b) the corresponding distributions of water saturation along the flow direction under different overall saturation values.

So far, we have shown that our dynamic pore-network model can adequately predict the spontaneous imbibition in a complex porous medium, in comparison to VOF-based direct numerical simulations. In this subsection, we extend the comparison to the case with a more viscous nonwetting phase. Fig. 10a shows the comparison of the imbibition rates predicted by the VOF model and the pore-network model for an oil-water system. The viscosity ratio is assumed to be unity. The static contact angle used in the VOF model is 60°, while the revised contact angle used in the pore-network model is 69.8°. It is seen that the imbibition predicted by the pore-network model is much slower. In comparison to the air-water system, oil is more viscous and much harder to be displaced so that the water front advances much slower. This enhances numerical diffusion at the wetting front in our pore-network model as explained for Fig. 9. Fig. 10b shows the corresponding distributions of water saturation along the flow direction under different overall saturation values. The pore-network model clearly predicts much more diffusive wetting fronts in comparison to those predicted by the VOF model. This explains why the pore-network model underestimates the imbibition rate for the oil-water system.

Since benchmark data of spontaneous imbibition for the verification of pore-scale models are absent in the open literature, in what follows, we compare the predictions of spontaneous imbibition rate by the VOF model and the single-phase Darcy model (Appendix A), given the fact that the single-phase Darcy model can well describe spontaneous imbibition of water into dry porous media (Cai et al., 2014; Kuijpers et al., 2017). The key assumption in the single-phase Darcy model is that a sharp wetting front holds in the imbibition process. As shown in Fig. 9 and Fig. 10b, sharp wetting fronts hold for both air-water and oil-water systems in the VOF simulations. The ordinary

differential equation (Eq. A6) for the imbibition rate is numerically solved by Matlab. We use the effective mean pore size to approximate the capillary pressure, which is given as $\tilde{R}^m = 1.2R^m$. R^m is the mean pore size given in Table 1. The water saturation behind the wetting front is set to 0.9. Fig. 11 shows the comparison of the imbibition rates predicted by the VOF model and the single-phase Darcy model (Eq. A6) under different viscosity ratios. It is seen that without revising the contact angle the Darcy model overestimates the imbibition rate considerably. However, after we revise the two contact angle values by Eq. 14, the imbibition curves predicted by the Darcy model can match the VOF-model predictions well even through the porous medium under study is much smaller than its REV (representative elementary volume) size. With the assumption of a sharp wetting front, the Darcy model can predicts the imbibition rate well for the oil-water system. This supports the conjecture that the pore-network work underestimates the imbibition rate for the oil-water system due to numerical diffusion at the wetting front.

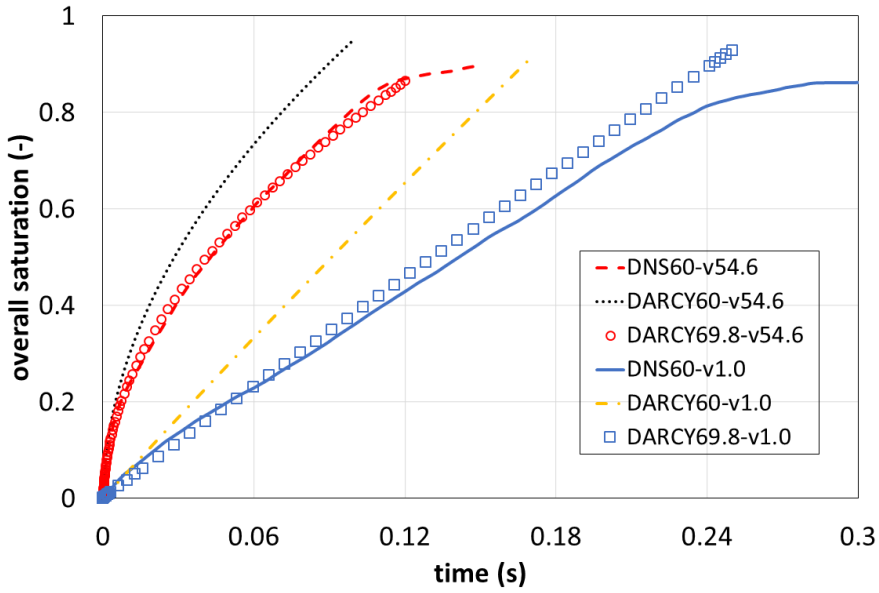

Fig. 11: Comparison of the imbibition rates predicted by the VOF model and the single-phase Darcy model (Eq. A6) under different viscosity ratios. The notation of '*Darcy60-v54.6*' in the legend detonates the case study by the Darcy model, for the air-water system with the contact angle of 60° and the viscosity ratio of 54.6.

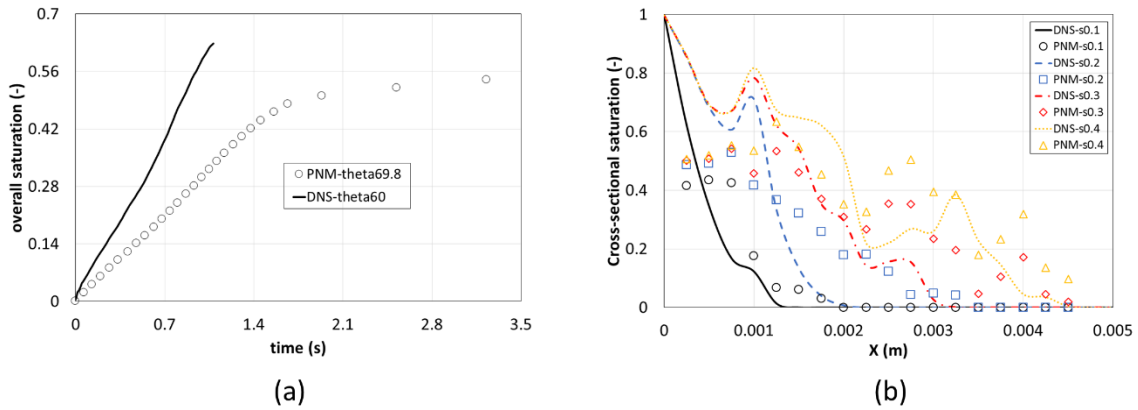

(a) (b)

Fig. 12: (a) Comparison of the imbibition rates predicted by the VOF model and the pore-network model for a highly viscous nonwetting phase. The nonwetting viscosity is 1.0×10^{-2} Pa s. (b) the corresponding distributions of water saturation along the flow direction under different overall saturation values.

We further increase the viscosity of the nonwetting phase to 0.01 Pa s to test the dynamic pore-network model. Fig. 12a shows the comparison of the imbibition rates predicted by the VOF model and the pore-network model for the viscosity ratio of 0.1. As expected, the imbibition rate predicted by the pore-network model is slower in comparison to the VOF model. Moreover, significant discrepancy is found among the water distribution profiles predicted by the pore-network model and the VOF model as shown in Fig. 12b. Obviously, the pore-network model predicts much more diffusive wetting fronts, causing unrealistic saturation-profile predictions in this case study.

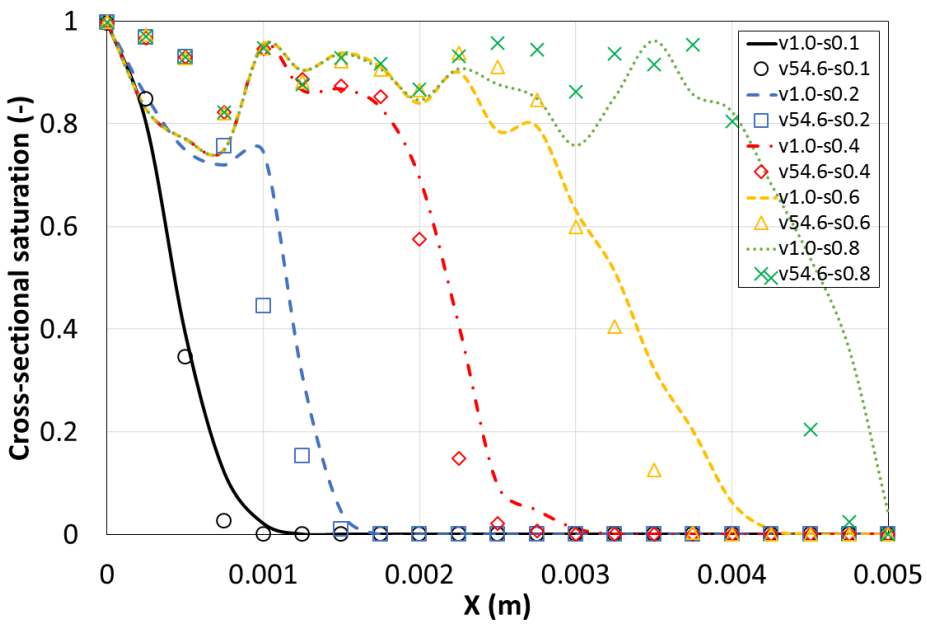

Fig. 13: Distributions of the water saturation along the flow direction under different overall saturation values for both air-water and oil-water systems predicted by the VOF model. The static contact angle used in the VOF model is 60°.

Finally, we discuss about the effect of the viscosity ratio of the wetting to the nonwetting phases on the roughness of wetting fronts. This influences the trapping of the nonwetting phase in spontaneous imbibition. For the air-water system, the wetting phase itself depresses the roughness growth of the wetting front (Gruener et al., 2012), while much less viscous air does not play a role. Both experimental data (Akin et al., 2000; Kuijpers et al., 2017) and numerical results in this work show that a sharp wetting front advances through porous media. Moreover, a sharp wetting front is maintained over a long distance (Alyafei et al., 2016; Schmid et al., 2016). For the oil-water system, the nonwetting phase, oil, is much more viscous. In principle, it assists the roughness growth of the wetting front so that a diffusion-type wetting front is seen in the distribution of wetting saturation along the flow direction (Schembre and Kovscek, 1998). If the nonwetting viscosity continues to increase, the wetting front will switch to a viscous-finger distribution. Fig. 13 shows the distributions of water saturation along the flow direction under different overall saturation values for both air-water and oil-water systems predicted by the VOF model. Here, we do see a rougher wetting front for the oil-water system even through it is slight. We expect that for a much longer porous medium the roughness of the wetting front for the oil-water system will continue to grow along the flow direction (Akin et al., 2000).

6. Conclusions

The pore-network modeling of porous media has the key advantage of computational efficiency. In this work, we have compared and verified a dynamic pore-network model of spontaneous imbibition against VOF simulations. In light of computational efforts of the VOF model, a small piece of μCT scanning of sintered glass beads has been used as our study domain. With the help of the open-source extraction code, PoreSpy, we prepared the pore network, which adequately represents the porous medium under study. A number of case studies of the primary imbibition by both dynamic pore-network model and VOF model have been conducted under different contact angle values and viscosity ratios. Based on those case studies, we arrive at the following main conclusions:

1. It is challenging for the VOF model to simulate spontaneous imbibition in a strongly or weakly water-wet porous medium, which is represented by pore-space voxels.
2. Voxel-induced roughness in the voxel representation of a porous medium slows down the imbibition process in comparison to the imbibition in the smooth-geometry representation. To mitigate the impact of voxel-induced roughness on the imbibition rate, one may revise the contact angle as in Eq. 14.
3. By using revised contact angle values, for the air-water system our pore-network model can predict imbibition rates and temporal saturation profiles along the flow direction well, in comparison to the VOF simulations.
4. For the oil-water system, due to numerical diffusion at the wetting front, our pore-network model predicts a slower imbibition process in comparison to the VOF model. Meanwhile, the predicted wetting front is rougher.
5. Our pore-network model is much more computationally efficient than the VOF model. The pore-network model running on a single core takes less than one minute for one case study, while the VOF model typically needs around one week of 16-core parallel computation.

Acknowledgment

This work is part of the research programme 'Fundamental Fluid Dynamic Challenges in Inkjet Printing' with project number FIP11, which is financed by the Dutch Research Council (NWO). The support of Océ Technologies within this program is acknowledged. C.Z.Q. acknowledges the support of Darcy Center of Utrecht University and Eindhoven University of Technology. The dataset associated with the present work is available via https://doi.org/10.6084/m9.figshare.10093676.

Aghaei, A., Piri, M., 2015. Direct pore-to-core up-scaling of displacement processes: Dynamic pore network modeling and experimentation. J. Hydrol. 522, 488–509. https://doi.org/10.1016/j.jhydrol.2015.01.004

Akin, S., Schembre, J.M., Bhat, S.K., Kovscek, A.R., 2000. Spontaneous imbibition characteristics of diatomite. J. Pet. Sci. Eng. 25, 149–165. https://doi.org/10.1016/S0920-4105(00)00010-3

Alyafei, N., Al-Menhali, A., Blunt, M.J., 2016. Experimental and Analytical Investigation of Spontaneous Imbibition in Water-Wet Carbonates. Transp. Porous Media 115, 189–207. https://doi.org/10.1007/s11242-016-0761-4

Brackbill, J.U., Kothe, D.B., Ridge, O., 1992. A Continuum Method for Modeling Surface Tension A Continuum Method for Modeling Surface Tension 9991. https://doi.org/10.1016/0021-9991(92)90240-Y

Cai, J., Perfect, E., Cheng, C.L., Hu, X., 2014. Generalized modeling of spontaneous imbibition based on hagen-poiseuille flow in tortuous capillaries with variably shaped apertures. Langmuir 30, 5142–5151. https://doi.org/10.1021/la5007204

Ferrari, A., Jimenez-Martinez, J., Le Borgne, T., Mèheust, Y., Lunati, I., 2015. Challenges inmodeling unstable two-phase flow experiments in porousmicromodels. Water Resour. Res. 51, 1381–1400. https://doi.org/10.1002/2014WR016384.Received

Forsberg, P.S.H., Priest, C., Brinkmann, M., Sedev, R., Ralston, J., 2010. Contact line pinning on microstructured surfaces for liquids in the Wenzel state. Langmuir 26, 860–865. https://doi.org/10.1021/la902296d

Gostick, J.T., 2017. Versatile and efficient pore network extraction method using marker-based watershed segmentation. Phys. Rev. E 96, 1–15. https://doi.org/10.1103/PhysRevE.96.023307

Gruener, S., Sadjadi, Z., Hermes, H.E., Kityk, A. V., Knorr, K., Egelhaaf, S.U., Rieger, H., Huber, P., 2012. Anomalous front broadening during spontaneous imbibition in a matrix with elongated pores. Proc. Natl. Acad. Sci. 109, 10245–10250. https://doi.org/10.1073/pnas.1119352109

Guo, B., Bandilla, K.W., Nordbotten, J.M., Celia, M.A., Keilegavlen, E., Doster, F., 2016. A multiscale multilayer vertically integrated model with vertical dynamics for CO2 sequestration in layered geological formations. Water Resour. Res. https://doi.org/10.1002/2016WR018714

Huang, X., Bandilla, K.W., Celia, M.A., 2016. Multi-Physics Pore-Network Modeling of Two-Phase Shale Matrix Flows. Transp. Porous Media 111, 123–141. https://doi.org/10.1007/s11242-015-0584-8

Hughes, R.G., Blunt, M.J., 2000. Pore Scale Modeling of Rate Effects in Imbibition. Transp. Porous Media 40, 295–322. https://doi.org/10.1023/A:1006629019153

Joekar-Niasar, V., Hassanizadeh, S.M., Dahle, H.K., 2010. Non-equilibrium effects in capillarity and interfacial area in two-phase flow: dynamic pore-network modelling. J. Fluid Mech. 655, 38–71. https://doi.org/10.1017/S0022112010000704

Kuijpers, C.J., Huinink, H.P., Tomozeiu, N., Erich, S.J.F., Adan, O.C.G., 2017. Sorption of water-glycerol mixtures in porous Al2O3 studied with NMR imaging. Chem. Eng. Sci. 173, 218–229. https://doi.org/10.1016/j.ces.2017.07.035

Kunz, P., Zarikos, I.M., Karadimitriou, N.K., Huber, M., Nieken, U., Hassanizadeh, S.M., 2016. Study of Multi-phase Flow in Porous Media: Comparison of SPH Simulations with Micro-model Experiments. Transp. Porous Media 114, 581–600. https://doi.org/10.1007/s11242-015-

0599-1

Li, J., McDougall, S.R., Sorbie, K.S., 2017. Dynamic pore-scale network model (PNM) of water imbibition in porous media. Adv. Water Resour. 107, 191–211. https://doi.org/10.1016/j.advwatres.2017.06.017

Liu, Y., Cai, J., Sahimi, M., Qin, C., 2020. A Study of the Role of Microfractures in Counter-Current Spontaneous Imbibition by Lattice Boltzmann Simulation. Transp. Porous Media 133, 313–332. https://doi.org/10.1007/s11242-020-01425-w

Mason, G., Morrow, N.R., 1991. Capillary behavior of a perfectly wetting liquid in irregular triangular tubes. J. Colloid Interface Sci. 141, 262–274. https://doi.org/10.1016/0021-9797(91)90321-X

Mayer, R.P., Stowe, R.A., 1965. Mercury porosimetry-breakthrough pressure for penetration between packed spheres. J. Colloid Sci. https://doi.org/10.1016/0095-8522(65)90061-9

Médici, E.F., Allen, J.S., 2013. Evaporation, two phase flow, and thermal transport in porous media with application to low-temperature fuel cells. Int. J. Heat Mass Transf. 65, 779–788. https://doi.org/10.1016/j.ijheatmasstransfer.2013.06.035

Mehmani, Y., Tchelepi, H.A., 2017. Minimum requirements for predictive pore-network modeling of solute transport in micromodels. Adv. Water Resour. 108, 83–98. https://doi.org/10.1016/j.advwatres.2017.07.014

Morrow, N.R., Mason, G., 2001. Recovery of oil by spontaneous imbibition. Curr. Opin. Colloid Interface Sci. 6, 321–337. https://doi.org/10.1016/S1359-0294(01)00100-5

Nguyen, V.H., Sheppard, A.P., Knackstedt, M.A., Val Pinczewski, W., 2006. The effect of displacement rate on imbibition relative permeability and residual saturation. J. Pet. Sci. Eng. 52, 54–70. https://doi.org/10.1016/j.petrol.2006.03.020

Patzek, T.W., 2001. Verification of a Complete Pore Network Simulator of Drainage and Imbibition. SPE J. 6, 144–156. https://doi.org/10.2118/71310-PA

Patzek, T.W., Kristensen, J.G., 2001. Shape Factor Correlations of Hydraulic Conductance in Noncircular Capillaries: I. One-Phase Creeping Flow. J. Colloid Interface Sci. 236, 295–304. https://doi.org/10.1006/jcis.2000.7414

Pavuluri, S., Doster, F., Maes, J., Yang, J., Regaieg, M., Moncorg, A., 2019. Towards pore network modelling of spontaneous imbibition : contact angle dependent invasion patterns and the occurrence of dynamic capillary barriers. Comput. Geosci.

Princen, H.M., 1970. Capillary phenomena in assemblies of parallel cylinders. III. Liquid Columns between Horizontal Parallel Cylinders. J. Colloid Interface Sci. https://doi.org/10.1016/0021-9797(70)90167-0

Qin, C.-Z., Guo, B., Celia, M., Wu, R., 2019. Dynamic pore-network modeling of air-water flow through thin porous layers. Chem. Eng. Sci. 202, 194–207. https://doi.org/10.1016/j.ces.2019.03.038

Qin, C.-Z., Hassanizadeh, S.M., 2015. Pore-Network Modeling of Solute Transport and Biofilm Growth in Porous Media. Transp. Porous Media 110, 345–367. https://doi.org/10.1007/s11242-015-0546-1

Qin, C.-Z., van Brummelen, H., 2019. A dynamic pore-network model for spontaneous imbibition in

porous media. Adv. Water Resour. 133, 103420. https://doi.org/10.1016/j.advwatres.2019.103420

Qin, C., 2015. Water Transport in the Gas Diffusion Layer of a Polymer Electrolyte Fuel Cell: Dynamic Pore-Network Modeling. J. Electrochem. Soc. 162, F1036–F1046. https://doi.org/10.1149/2.0861509jes

Rabbani, A., Ayatollahi, S., Kharrat, R., Dashti, N., 2016. Estimation of 3-D pore network coordination number of rocks from watershed segmentation of a single 2-D image. Adv. Water Resour. 94, 264–277. https://doi.org/10.1016/j.advwatres.2016.05.020

Raeini, A.Q., Blunt, M.J., Bijeljic, B., 2014. Direct simulations of two-phase flow on micro-CT images of porous media and upscaling of pore-scale forces. Adv. Water Resour. 74, 116–126. https://doi.org/10.1016/j.advwatres.2014.08.012

Raeini, A.Q., Yang, J., Bondino, I., Bultreys, T., Blunt, M.J., Bijeljic, B., 2019. Validating the Generalized Pore Network Model Using Micro-CT Images of Two-Phase Flow. Transp. Porous Media 130, 405–424. https://doi.org/10.1007/s11242-019-01317-8

Schembre, J., Kovscek, A.R., 1998. spontaneous imbibition in low permeability media. SUPRI TR 114 Rep.

Schmid, K.S., Alyafei, N., Geiger, S., Blunt, M.J., 2016. Analytical Solutions for Spontaneous Imbibition: Fractional-Flow Theory and Experimental Analysis. SPE J. 21, 2308–2316. https://doi.org/10.2118/184393-pa

Shams, M., Raeini, A.Q., Blunt, M.J., Bijeljic, B., 2018. A numerical model of two-phase flow at the micro-scale using the volume-of-fluid method. J. Comput. Phys. 357. https://doi.org/10.1016/j.jcp.2017.12.027

Sheng, Q., Thompson, K., 2016. A unified pore-network algorithm for dynamic two-phase flow. Adv. Water Resour. 95, 92–108. https://doi.org/10.1016/j.advwatres.2015.12.010

Shokrpour Roudbari, M., van Brummelen, E.H., Verhoosel, C. V., 2016. A multiscale diffuse-interface model for two-phase flow in porous media. Comput. Fluids 141, 212–222. https://doi.org/10.1016/j.compfluid.2016.07.006

Sun, Y., Kharaghani, A., Tsotsas, E., 2016. Micro-model experiments and pore network simulations of liquid imbibition in porous media. Chem. Eng. Sci. 150, 41–53. https://doi.org/10.1016/j.ces.2016.04.055

Sweijen, T., Nikooee, E., Hassanizadeh, S.M., Chareyre, B., 2016. The Effects of Swelling and Porosity Change on Capillarity: DEM Coupled with a Pore-Unit Assembly Method. Transp. Porous Media 113, 207–226. https://doi.org/10.1007/s11242-016-0689-8

T. Hoang, C.V. Verhoosel, C. Qin, F. Auricchio, A. Reali, H. van Brummelen, 2018. Skeleton-stabilized ImmersoGeometric Analysis for incompressible viscous flow problems. Comput. Methods Appl. Mech. Engrg. 344, 421–450. https://doi.org/10.1016/j.cma.2018.10.015

Tørå, G., Øren, P.E., Hansen, A., 2012. A Dynamic Network Model for Two-Phase Flow in Porous Media. Transp. Porous Media 92, 145–164. https://doi.org/10.1007/s11242-011-9895-6

Valvatne, P.H., Blunt, M.J., 2004. Predictive pore-scale modeling of two-phase flow in mixed wet media. Water Resour. Res. 40, 1–21. https://doi.org/10.1029/2003WR002627

Wang, Sen, Feng, Q., Dong, Y., Han, X., Wang, Shoulei, 2015. A dynamic pore-scale network

model for two-phase imbibition. J. Nat. Gas Sci. Eng. 26, 118–129. https://doi.org/10.1016/j.jngse.2015.06.005

Yang, J., Bondino, I., Regaieg, M., Moncorgé, A., 2017. Pore to pore validation of pore network modelling against micromodel experiment results. Comput. Geosci. 21, 849–862. https://doi.org/10.1007/s10596-017-9630-7

Yi, Z., Lin, M., Jiang, W., Zhang, Z., Li, H., Gao, J., 2017. Pore network extraction from pore space images of various porous media systems. Water Resour. Res. 53, 3424–3445. https://doi.org/10.1002/2016WR019272

Yin, X., Zarikos, I., Karadimitriou, N.K., Raoof, A., Hassanizadeh, S.M., 2019. Direct simulations of two-phase flow experiments of different geometry complexities using Volume-of-Fluid (VOF) method. Chem. Eng. Sci. 195, 820–827. https://doi.org/10.1016/j.ces.2018.10.029

Yue, P., Feng, J.J., 2011. Wall energy relaxation in the Cahn-Hilliard model for moving contact lines. Phys. Fluids. https://doi.org/10.1063/1.3541806

Zhao, J., Qin, F., Derome, D., Carmeliet, J., 2020. Simulation of quasi-static drainage displacement in porous media on pore-scale: Coupling lattice Boltzmann method and pore network model. J. Hydrol. 588, 125080. https://doi.org/10.1016/j.jhydrol.2020.125080

Zhuang, L., Hassanizadeh, S.M., Qin, C.-Z., de Waal, A., 2017. Experimental Investigation of Hysteretic Dynamic Capillarity Effect in Unsaturated Flow. Water Resour. Res. 53, 9078–9088. https://doi.org/10.1002/2017WR020895

ANSYS, Inc. (2016) ANSYS Fluent User’s Guide, Release 17.2.

Appendix A:

Spontaneous imbibition into a porous medium initially saturated with the nonwetting phase

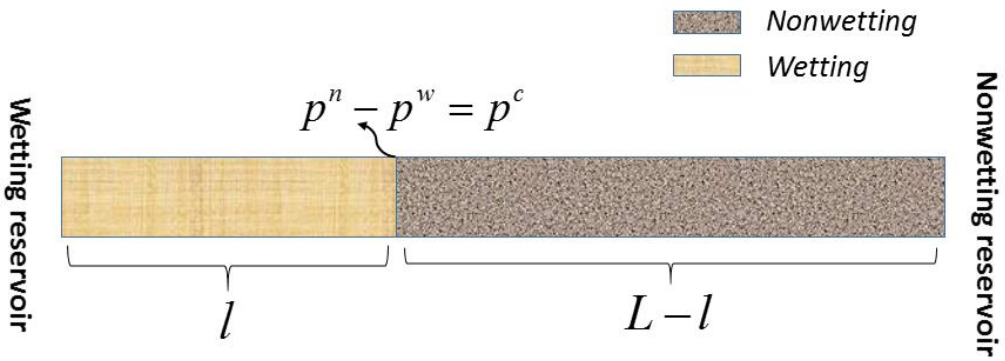

Fig. A1: Schematic of spontaneous imbibition into a dry porous medium at the Darcy scale.

By assuming a sharp wetting front, here we present the derivation of the 1D Darcy-scale model for spontaneous imbibition into a dry homogeneous porous medium as shown in Fig. A1. First, for the wetting phase, neglecting the gravity its Darcy flux is given as:

$$q^w = -\frac{k^w}{\mu^w}\frac{p^w}{l} \tag{A1}$$

where the superscript w denotes the wetting phase, q (m/s) is the flux, k (m^2) is the permeability, μ (Pa s) is the dynamic viscosity, l (m) is the wetting penetration length, and p (Pa) is the pressure. Then, we can write the rate of wetting saturation of the whole porous domain as follows:

$$AL\varepsilon\frac{dS}{dt} = -A\frac{k^w}{\mu^w}\frac{p^w}{l} \tag{A2}$$

where S is the wetting saturation of the whole porous domain, A is the cross-sectional area, L is the domain length, and ε is the porosity.

By virtue of volumetric conservation, and the condition of $p^n = p^c + p^w$ at the wetting front, we can write the nonwetting flux as:

$$q^n = q^w = \frac{k^n}{\mu^n}\frac{p^c+p^w}{L-l} \tag{A3}$$

Substitution of Eq. A1 into Eq. A3, and after some arithmetic manipulations, we can express the wetting phase pressure as:

$$p^w = -p^c\Big/\left(1+\frac{L-l}{l}\frac{k^w\mu^n}{k^n\mu^w}\right) \tag{A4}$$

Substitution of Eq. A4 into Eq. A2, we can obtain:

$$\frac{dS}{dt} = \frac{1}{L\varepsilon}\frac{k^w}{\mu^w}\frac{1}{l}\frac{p^c}{\left(1+\frac{L-l}{l}\frac{k^w\mu^n}{k^n\mu^w}\right)} \tag{A5}$$

We assume a constant wetting saturation of S^f behind the wetting front so that the wetting penetration length can be expressed as $l = SL/S^f$. Further, the wetting permeability is approximated by $k^w = k^0 S^f$ where k^0 is the intrinsic permeability. Because the medium is initially nonwetting-saturated, the nonwetting permeability is given by $k^n = k^0$. Finally, the ordinary differential equation for the imbibition rate is written as:

$$\frac{dS}{dt} = \frac{S^f}{L^2\varepsilon S}\frac{k^0 S^f}{\mu^w}\frac{p^c}{\left(1+\frac{S^f\mu^n}{\mu^w}\frac{S^f-S}{S}\right)} \tag{A6}$$

Appendix B:

Mass balance and capillary number in the pore-network simulations

Based on the constructed pore network, the discretized mass balance equation (4) is in the conservative form, which is solved by the first-order explicit scheme. To avoid extremely small time steps, at the end of each time step, we truncate the wetting saturation in a pore body as follows: when s_i^w is smaller than 10^{-6}, we set $s_i^w = 0$; when $(1 - s_i^w)$ is smaller than 10^{-6}, we set $s_i^w = 1$. This truncation practice may impact the mass imbalance. In our case studies, we calculate the mass imbalance of the wetting phase as:

$$\tilde{m}(t) = \left(\int_{t_0}^{t} \sum_{i=1}^{N} q_i^w - \sum_{i=1}^{N} V_i s_i^w \Big|_t\right) / \sum_{i=1}^{N} V_i \tag{B1}$$

where $\tilde{m}(t)$ is the mass imbalance at the imbibition time of t, q_i^w (m^3/s) is the net wetting flow rate of pore body i, and N is the number of pore bodies. Fig. B1 shows the wetting-phase mass imbalance in the pore-network modeling of spontaneous imbibition under different contact angle values and viscosity ratios. It is seen that for all case studies the mass imbalance is smaller than 10^{-3}, which is negligible. Furthermore, our case studies indicate that the truncation threshold has little impact on the mass imbalance.

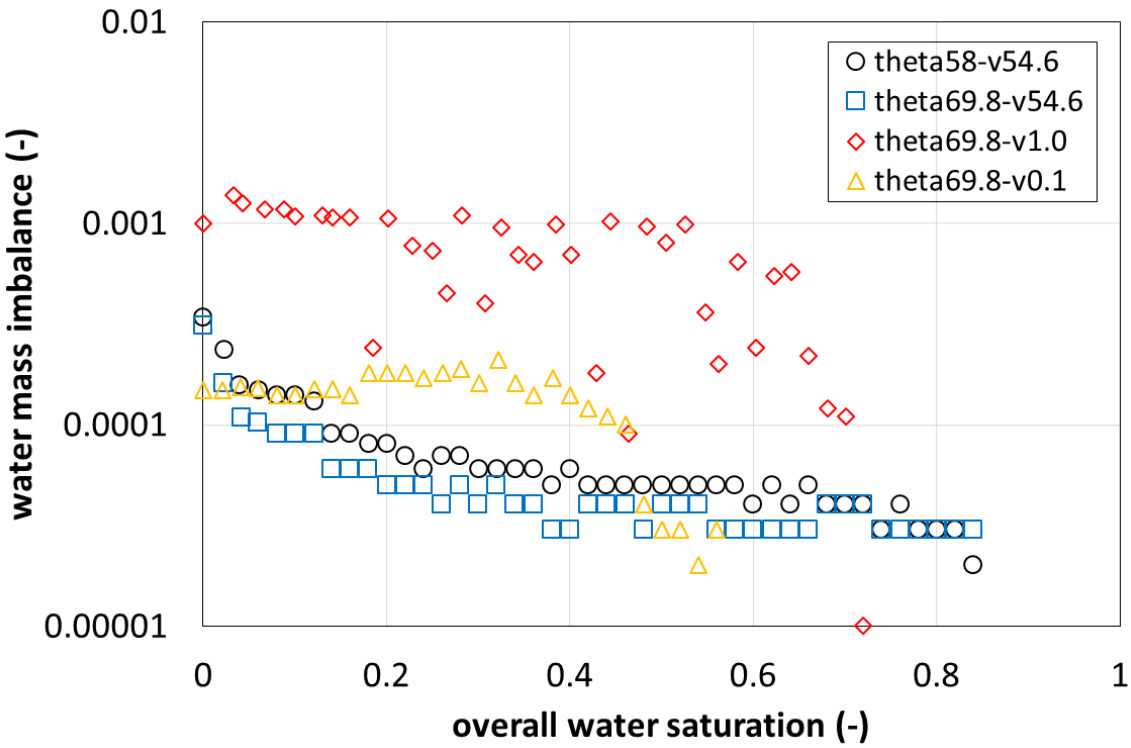

Fig. B1: Mass imbalance of the wetting phase in the pore-network modeling of spontaneous imbibition under different contact angle values and viscosity ratios.

Fig. B2 shows the temporal capillary number values in the pore-network modeling of spontaneous imbibition under different contact angle values and viscosity ratios. Obviously, for the air-water system, the capillary number decreases as the imbibition proceeds. At the viscosity ratio of unity, the capillary number keeps roughly constant before the wetting-phase breakthrough. At the viscosity ratio of 0.1, interestingly the capillary number also keeps roughly flat rather than increase, this is because the sharp wetting front does not hold any more (see Fig. 12b). Though the porous medium of sintered glass beads is highly permeable, for all case studies in this work the capillary number values are smaller than 10^{-3}. This indicates that the dynamic effect on the contact angle is minor. The wall roughness, however, would dominate the prediction uncertainties of spontaneous imbibition.

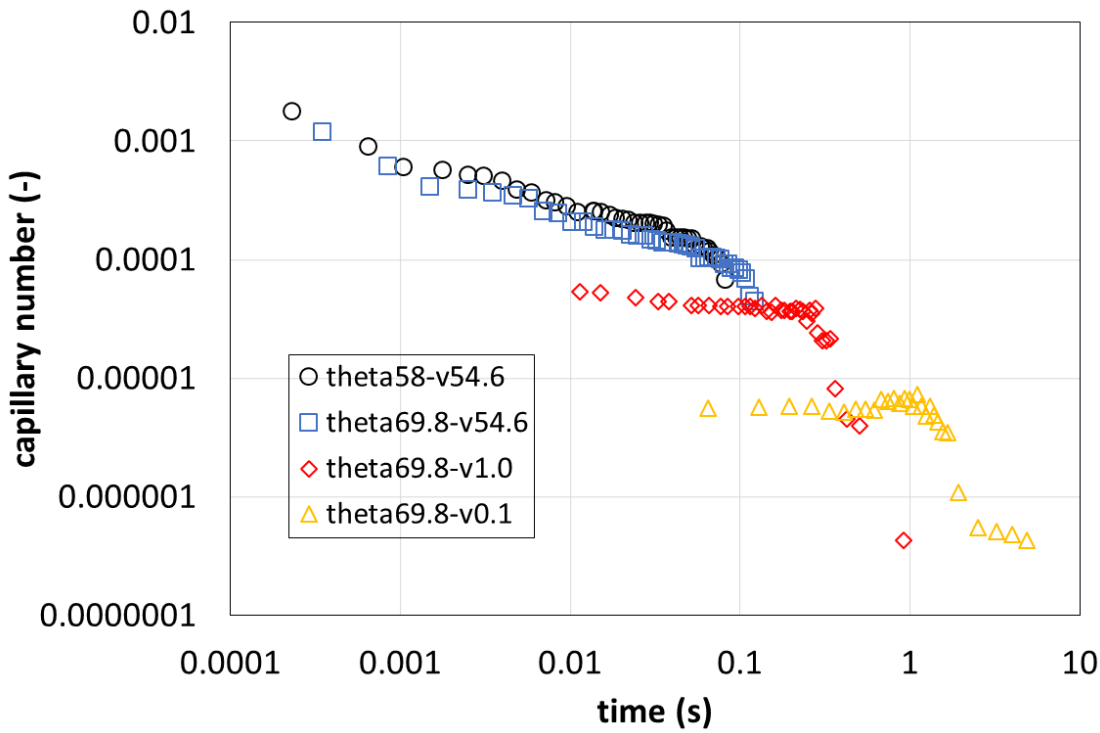

Fig. B2: Temporal capillary number values in the pore-network modeling of spontaneous imbibition under different contact angle values and viscosity ratios.

Figure 1.

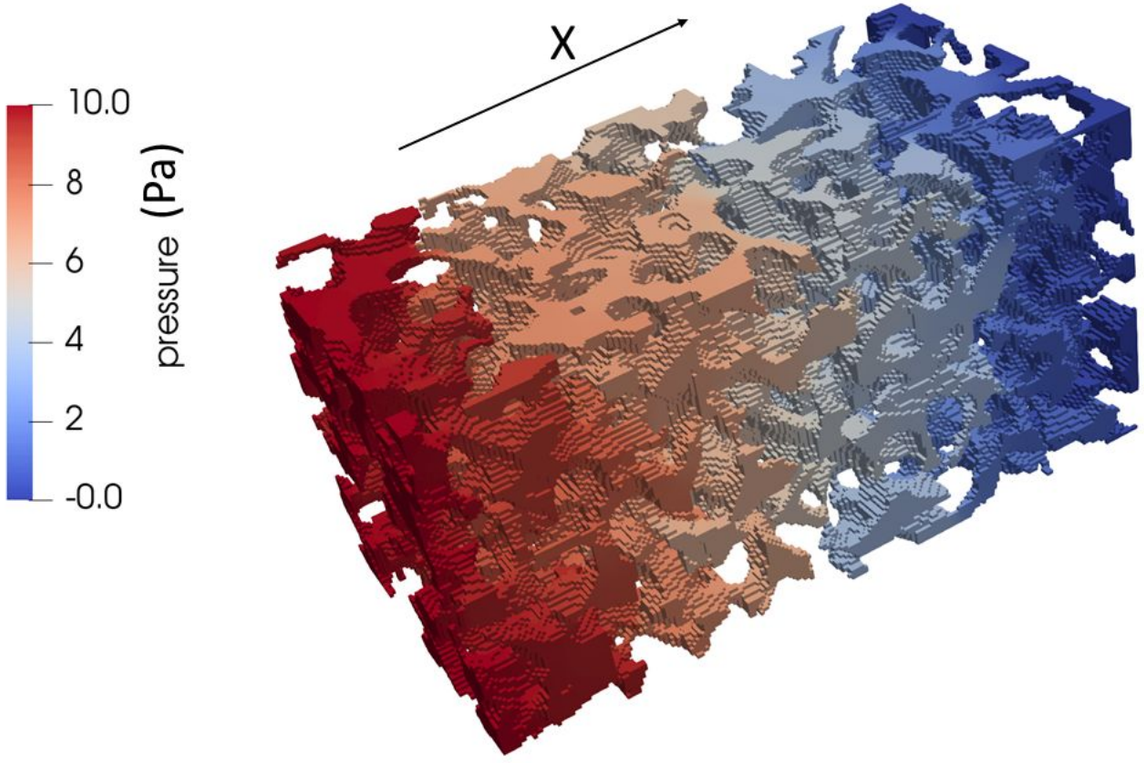
X
10.0
8
6
4
2
-0.0
pressure (Pa)

(a)

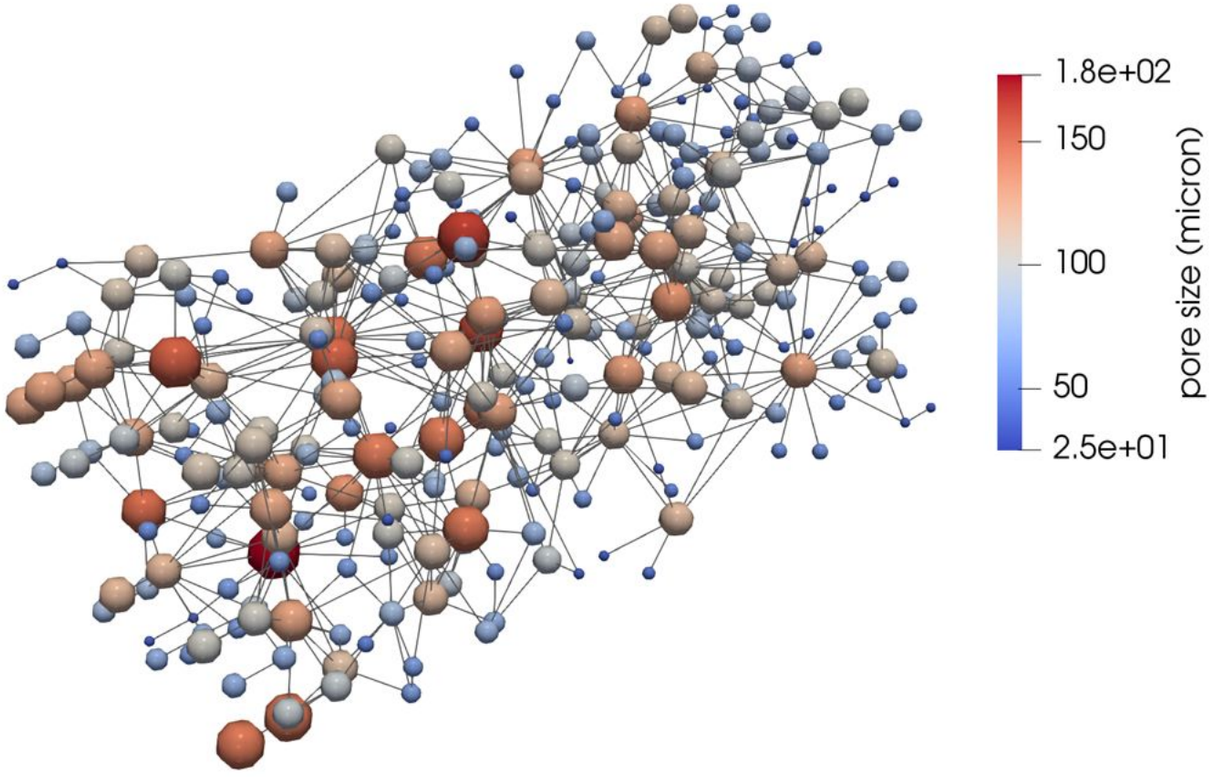
1.8e+02
150
100
50
2.5e+01
pore size (micron)

(b)

Figure 2.

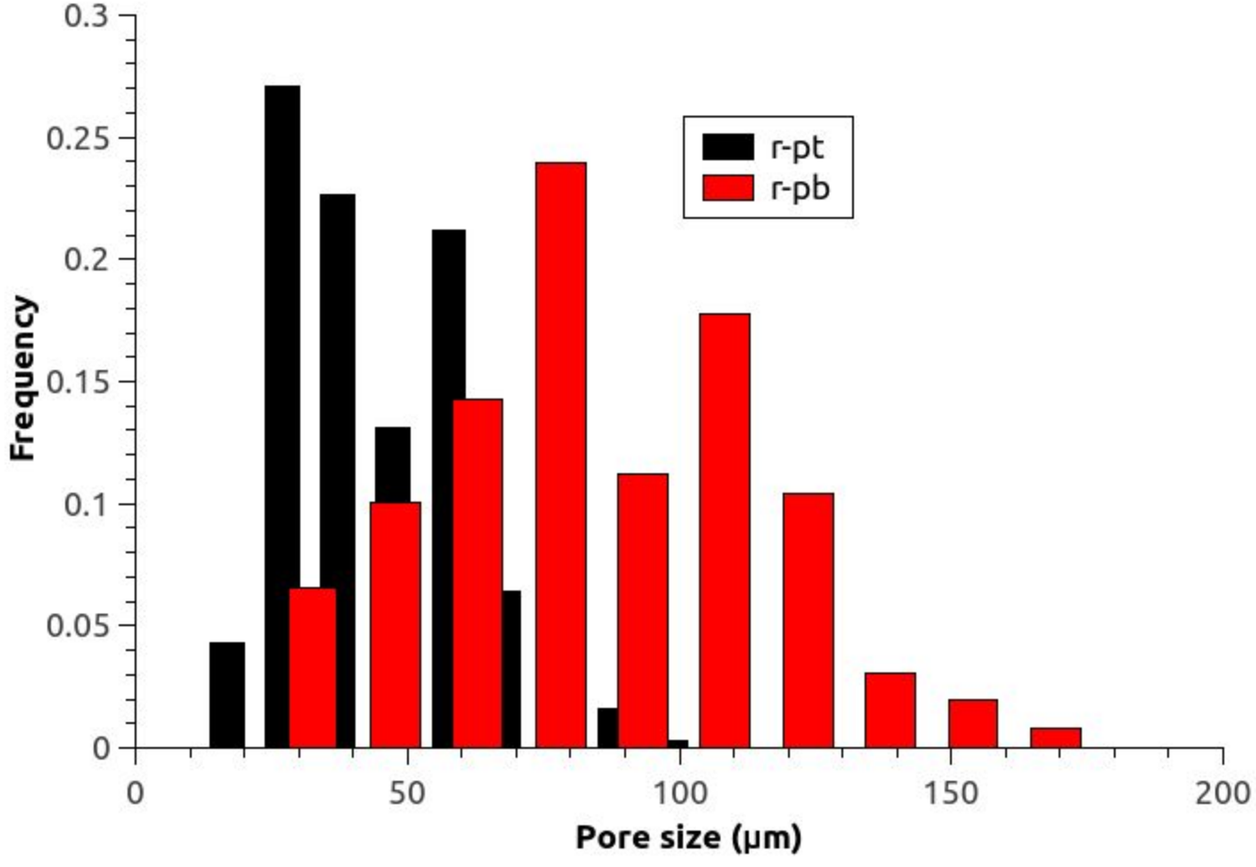
r-pt
r-pb
Frequency
Pore size (µm)
0
0.05
0.1
0.15
0.2
0.25
0.3
0
50
100
150
200

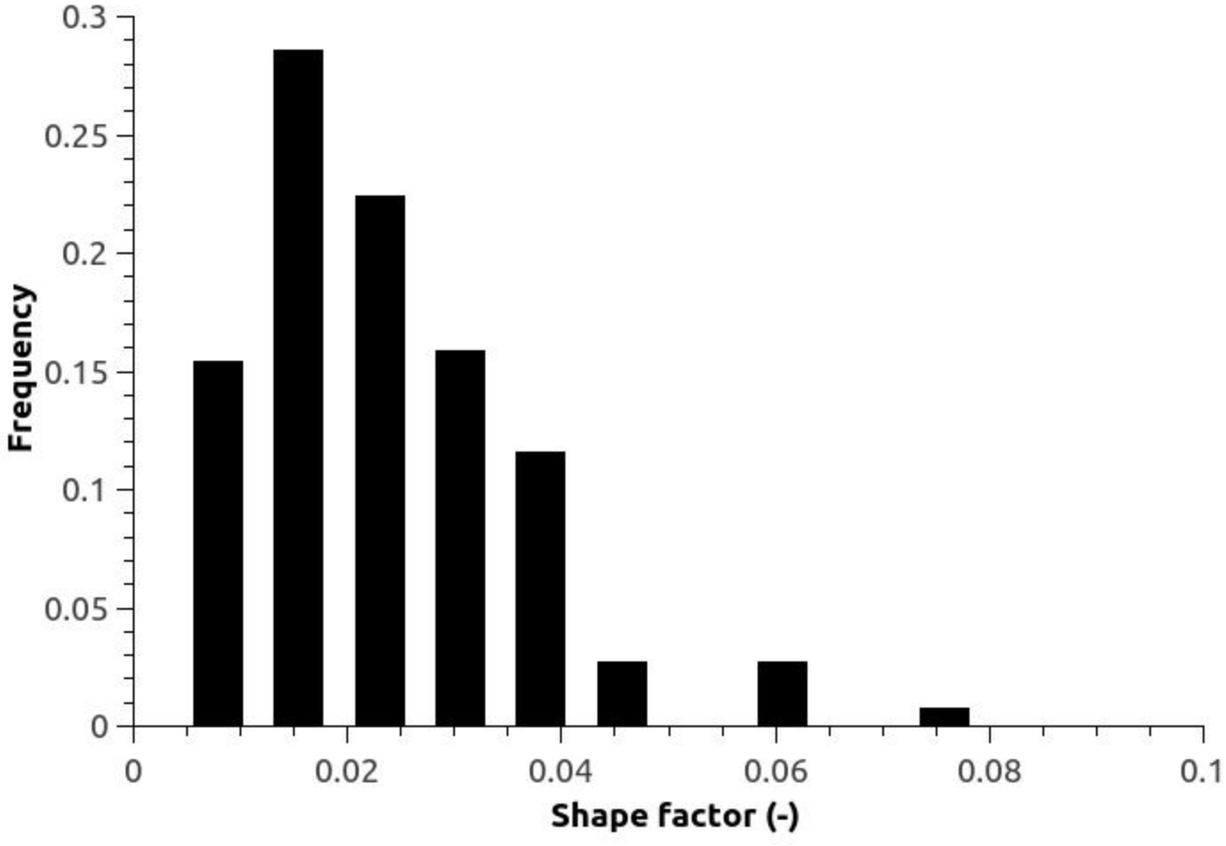
Frequency
Shape factor (-)
0
0.05
0.1
0.15
0.2
0.25
0.3
0
0.02
0.04
0.06
0.08
0.1

Figure 3.

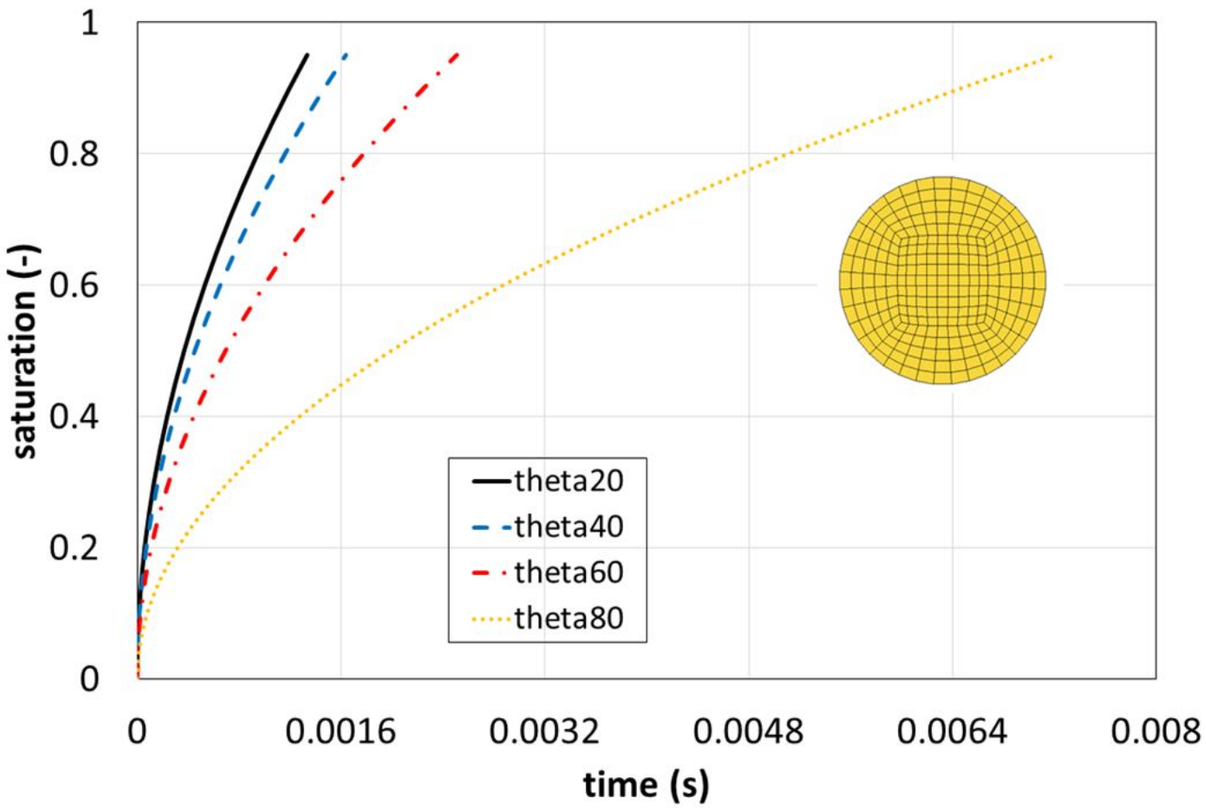
saturation (-)
time (s)
theta20
theta40
theta60
theta80

(a)

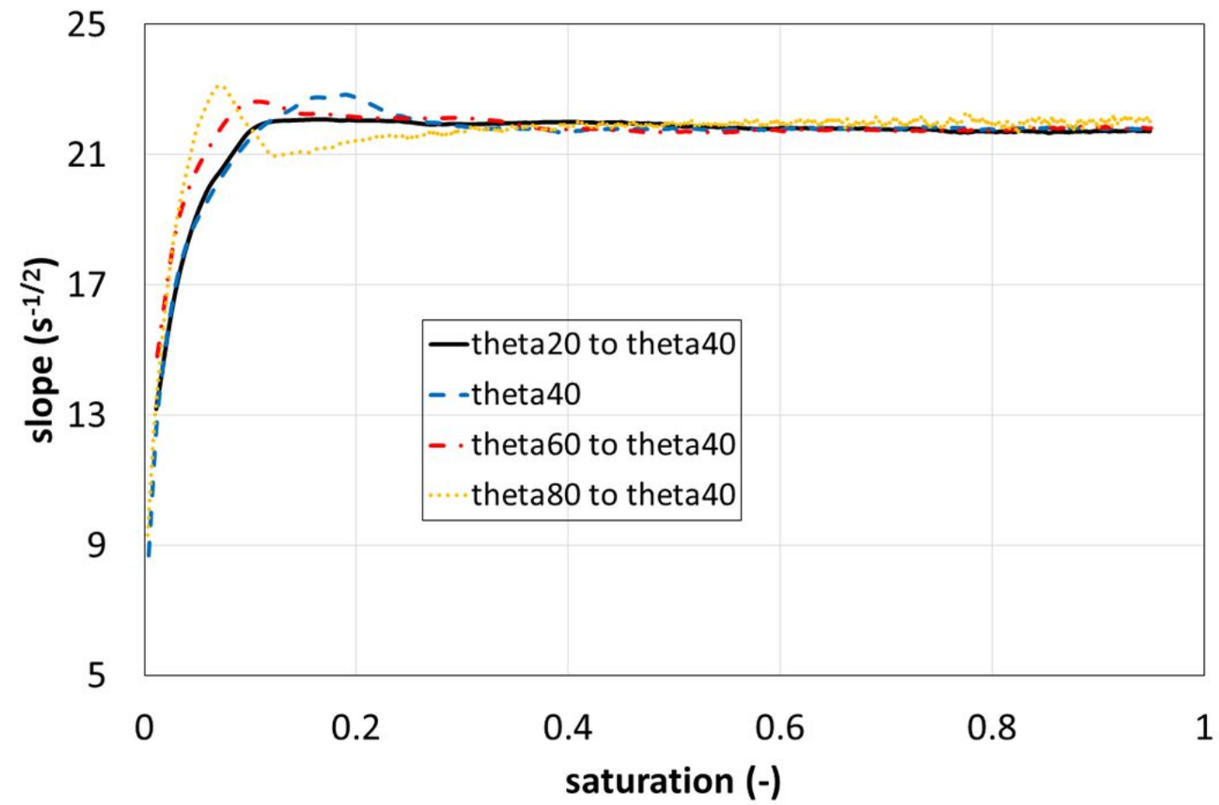
slope ($s^{-1/2}$)
saturation (-)
theta20 to theta40
theta40
theta60 to theta40
theta80 to theta40

(b)

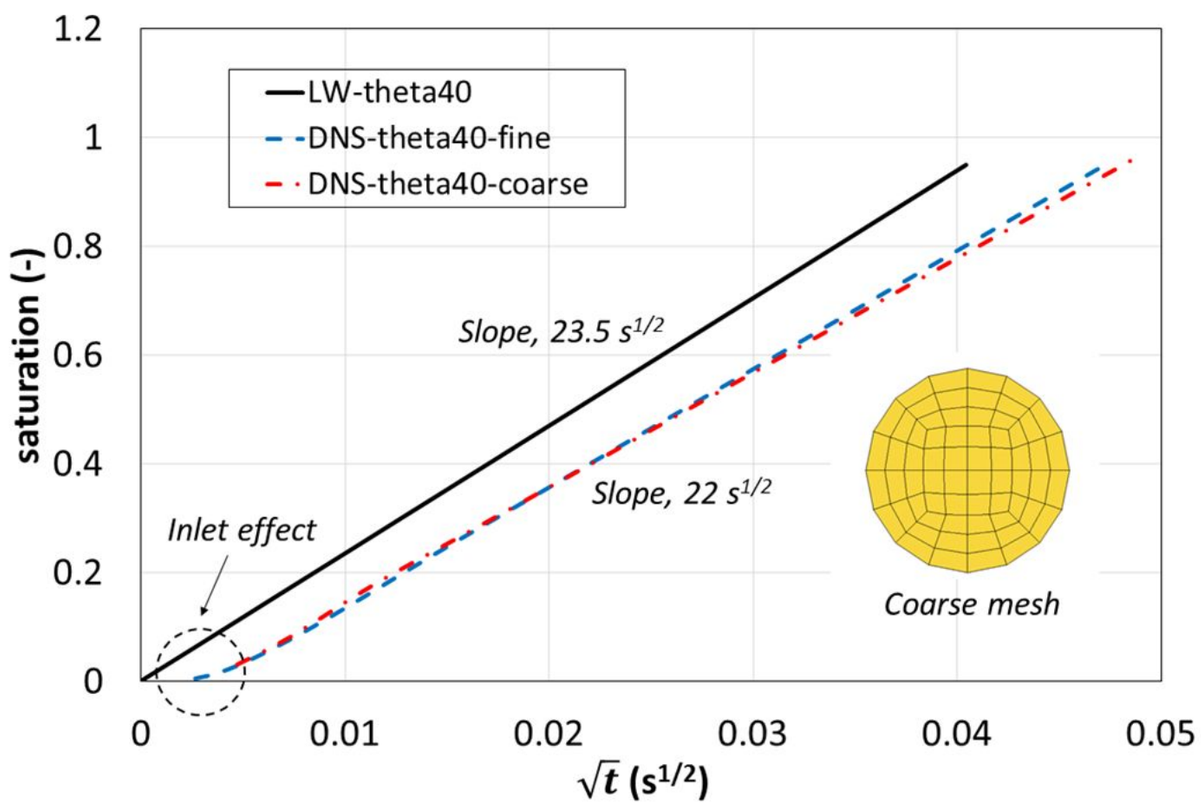
saturation (-)
$\sqrt{t}$ ($s^{1/2}$)
LW-theta40
DNS-theta40-fine
DNS-theta40-coarse
Slope, 23.5 $s^{1/2}$
Slope, 22 $s^{1/2}$
Inlet effect
Coarse mesh

(c)

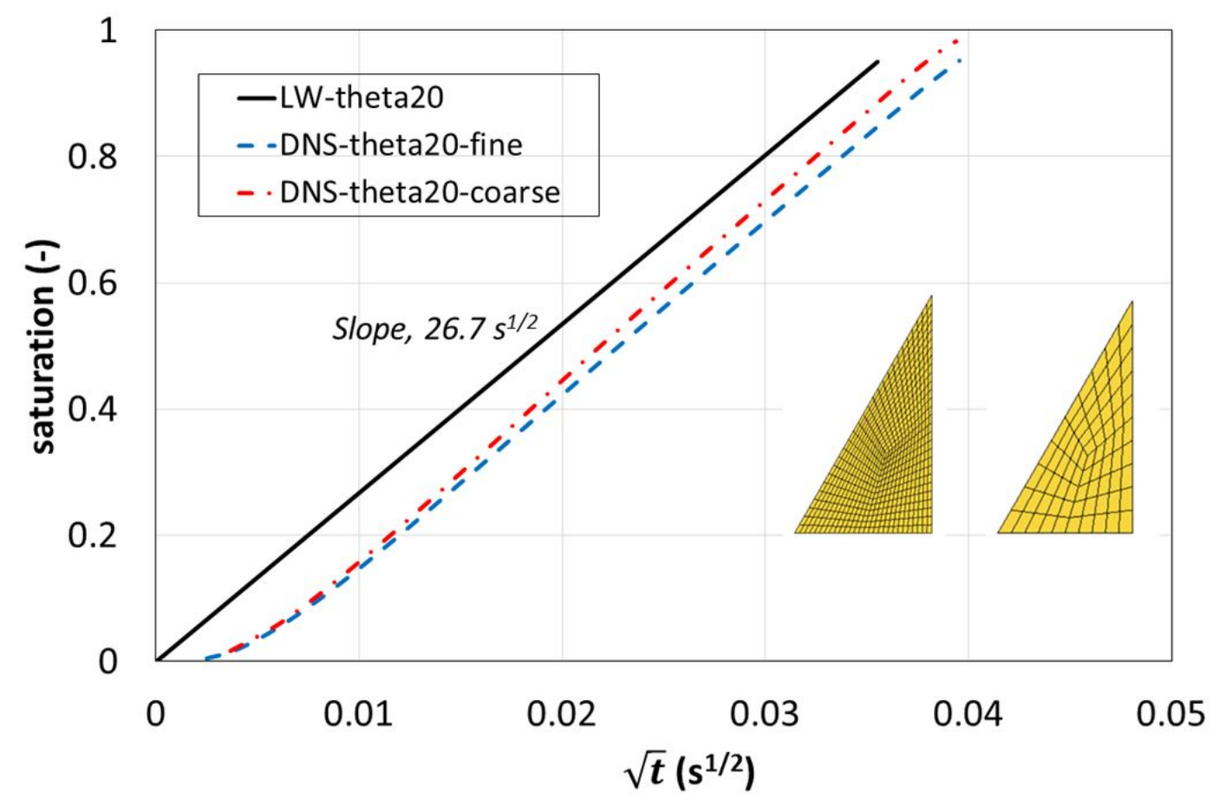
saturation (-)
$\sqrt{t}$ ($s^{1/2}$)
LW-theta20
DNS-theta20-fine
DNS-theta20-coarse
Slope, 26.7 $s^{1/2}$

(d)

Figure 4.

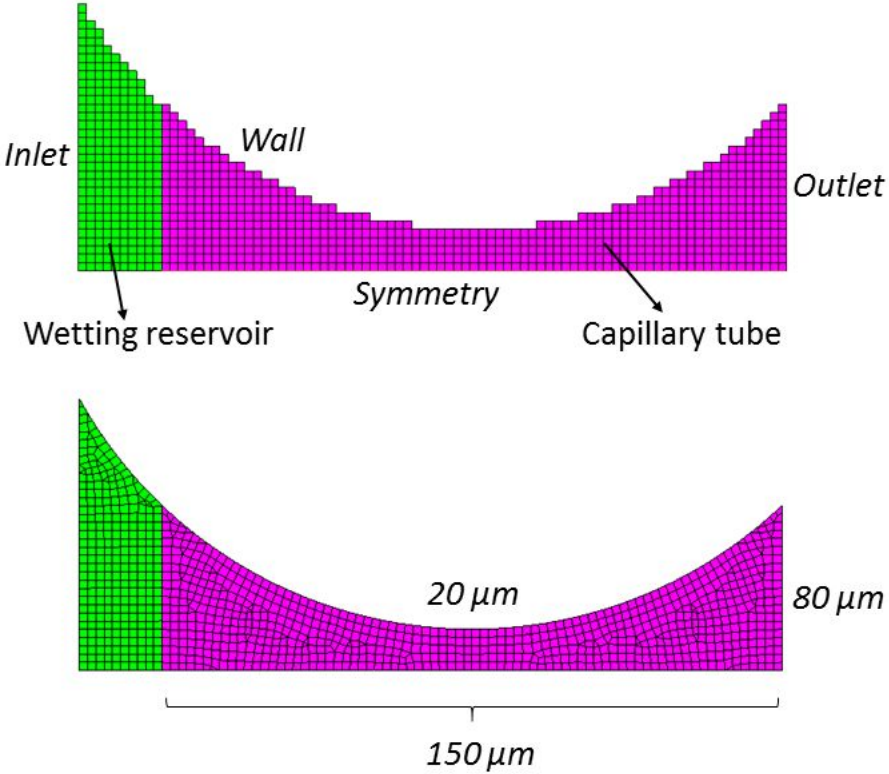
Inlet
Wall
Outlet
Symmetry
Wetting reservoir
Capillary tube
20 µm
80 µm
150 µm

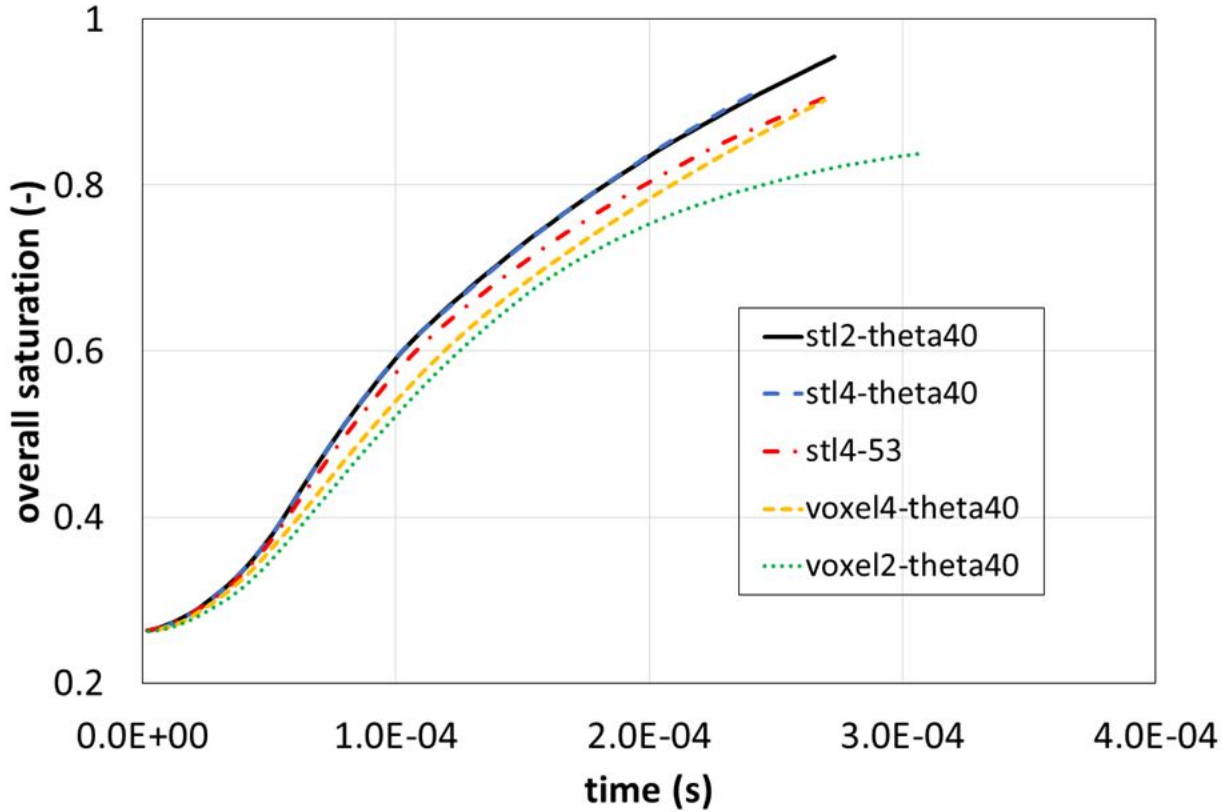
overall saturation (-)
time (s)
1
0.8
0.6
0.4
0.2
0.0E+00
1.0E-04
2.0E-04
3.0E-04
4.0E-04
stl2-theta40
stl4-theta40
stl4-53
voxel4-theta40
voxel2-theta40

Figure 5.

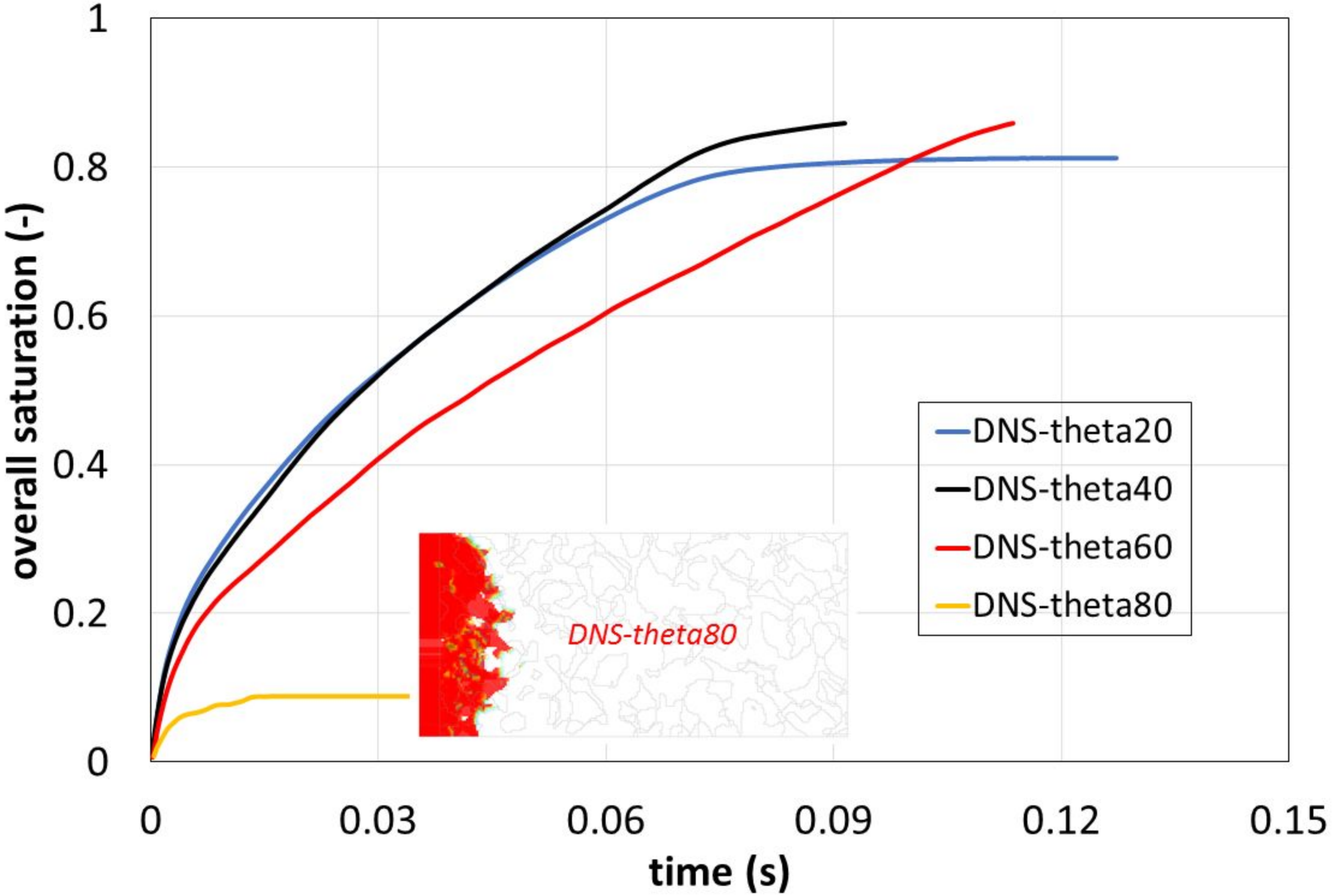
1
0.8
0.6
0.4
0.2
0
overall saturation (-)
0
0.03
0.06
0.09
0.12
0.15
time (s)
DNS-theta20
DNS-theta40
DNS-theta60
DNS-theta80
DNS-theta80

Figure 6.

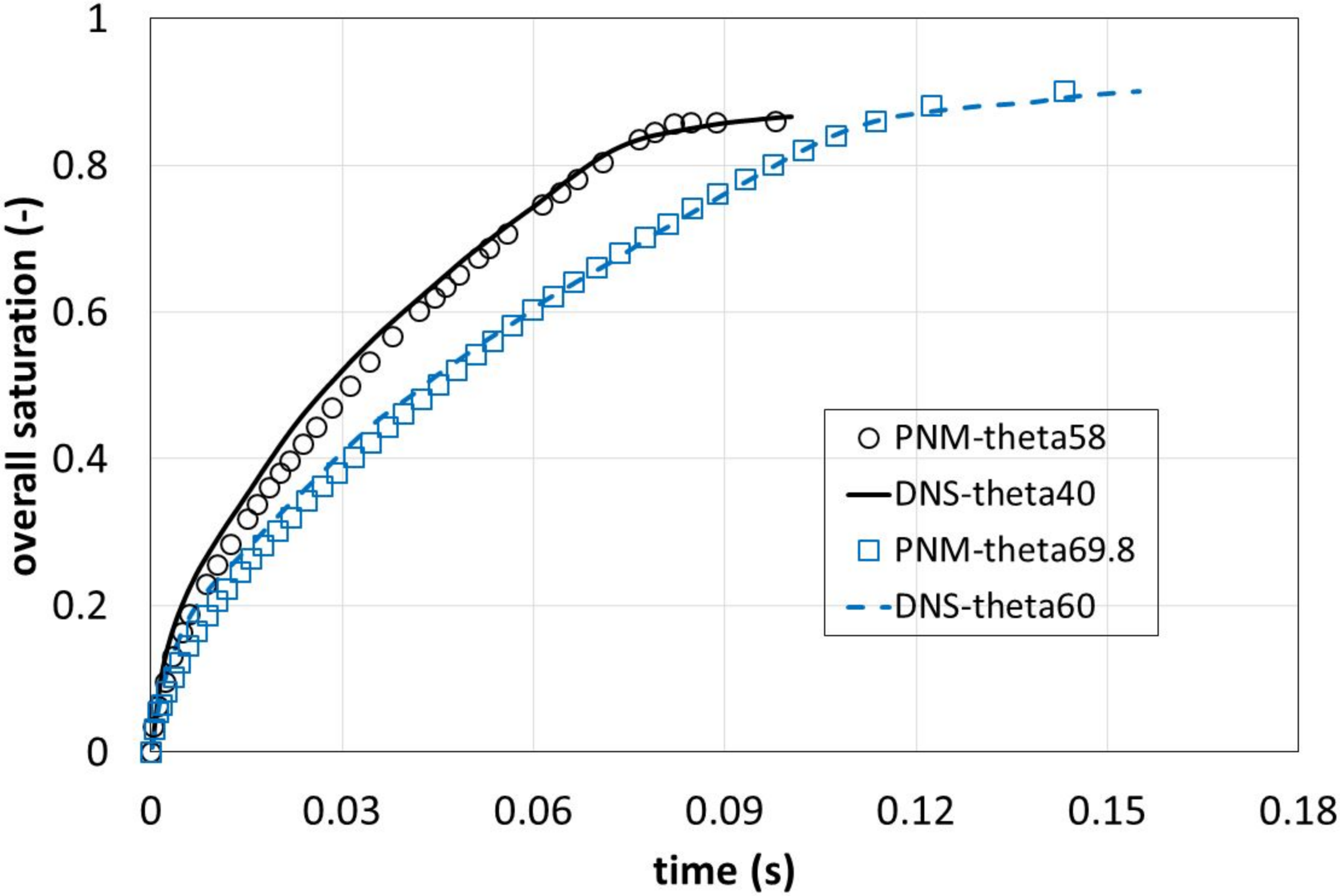
1
0.8
0.6
0.4
0.2
0
overall saturation (-)
0
0.03
0.06
0.09
0.12
0.15
0.18
time (s)
PNM-theta58
DNS-theta40
PNM-theta69.8
DNS-theta60

Figure 7.

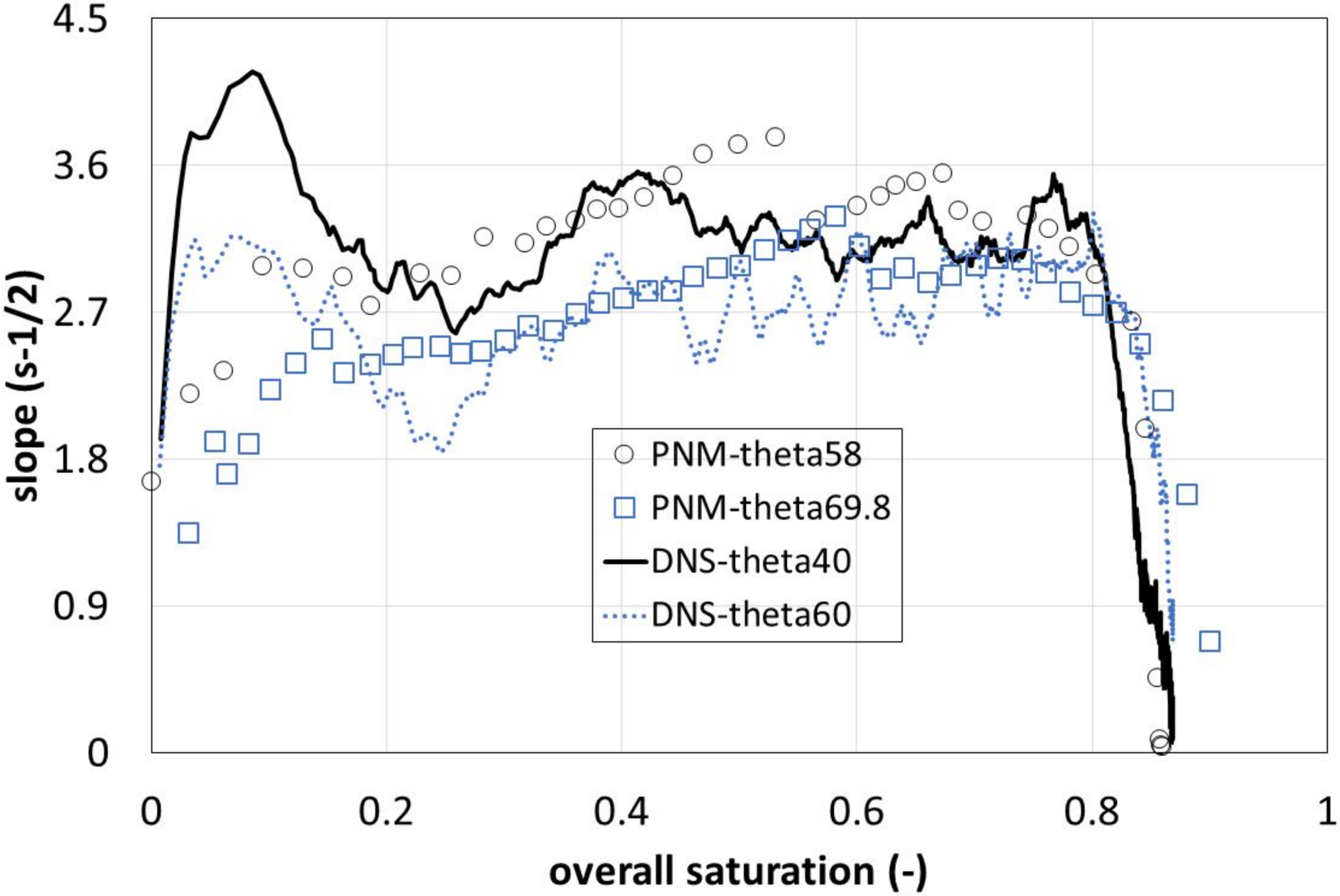
4.5
3.6
2.7
1.8
0.9
0
slope (s-1/2)
0
0.2
0.4
0.6
0.8
1
overall saturation (-)
PNM-theta58
PNM-theta69.8
DNS-theta40
DNS-theta60

Figure 8.

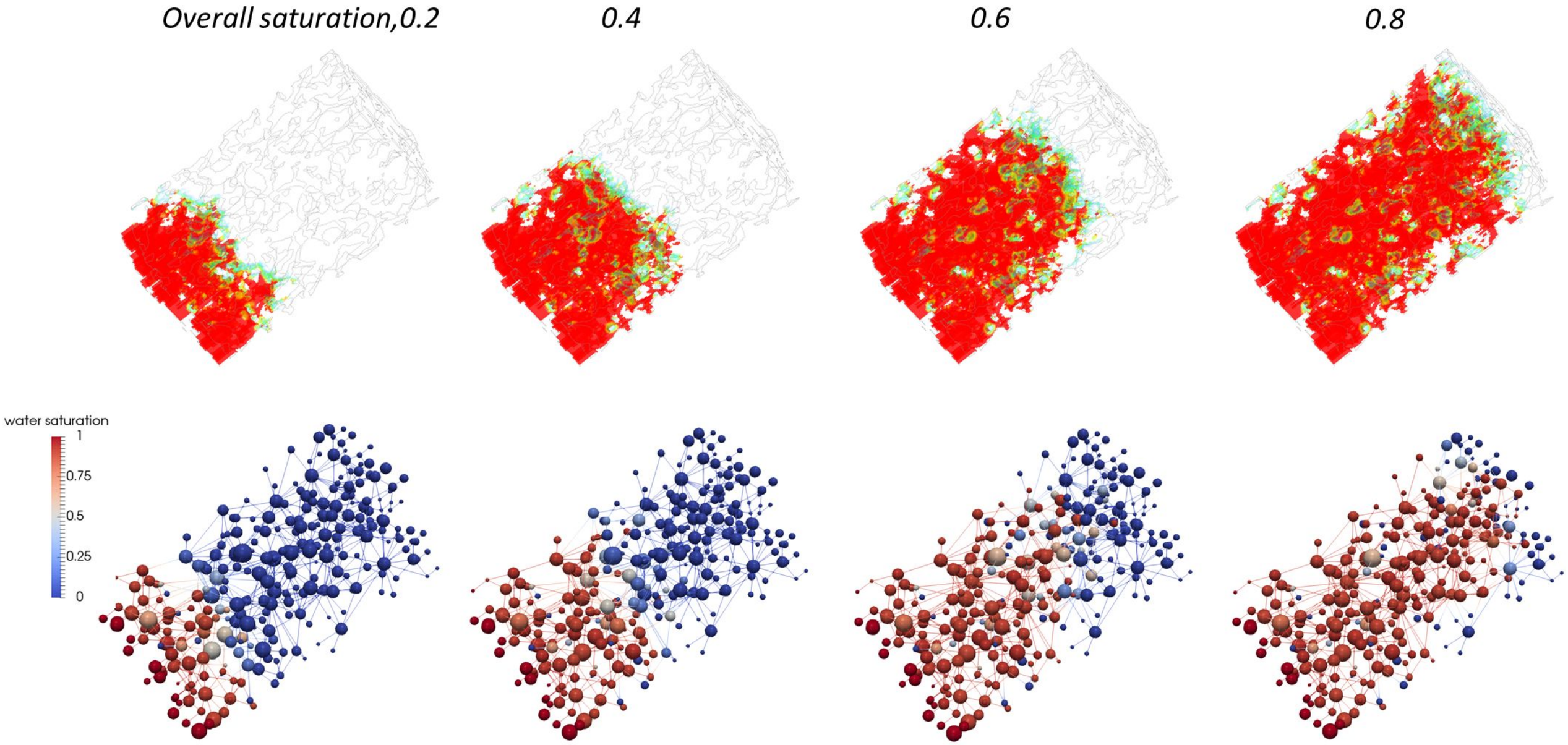
Overall saturation,0.2
0.4
0.6
0.8
water saturation
1
0.75
0.5
0.25
0

Figure 9.

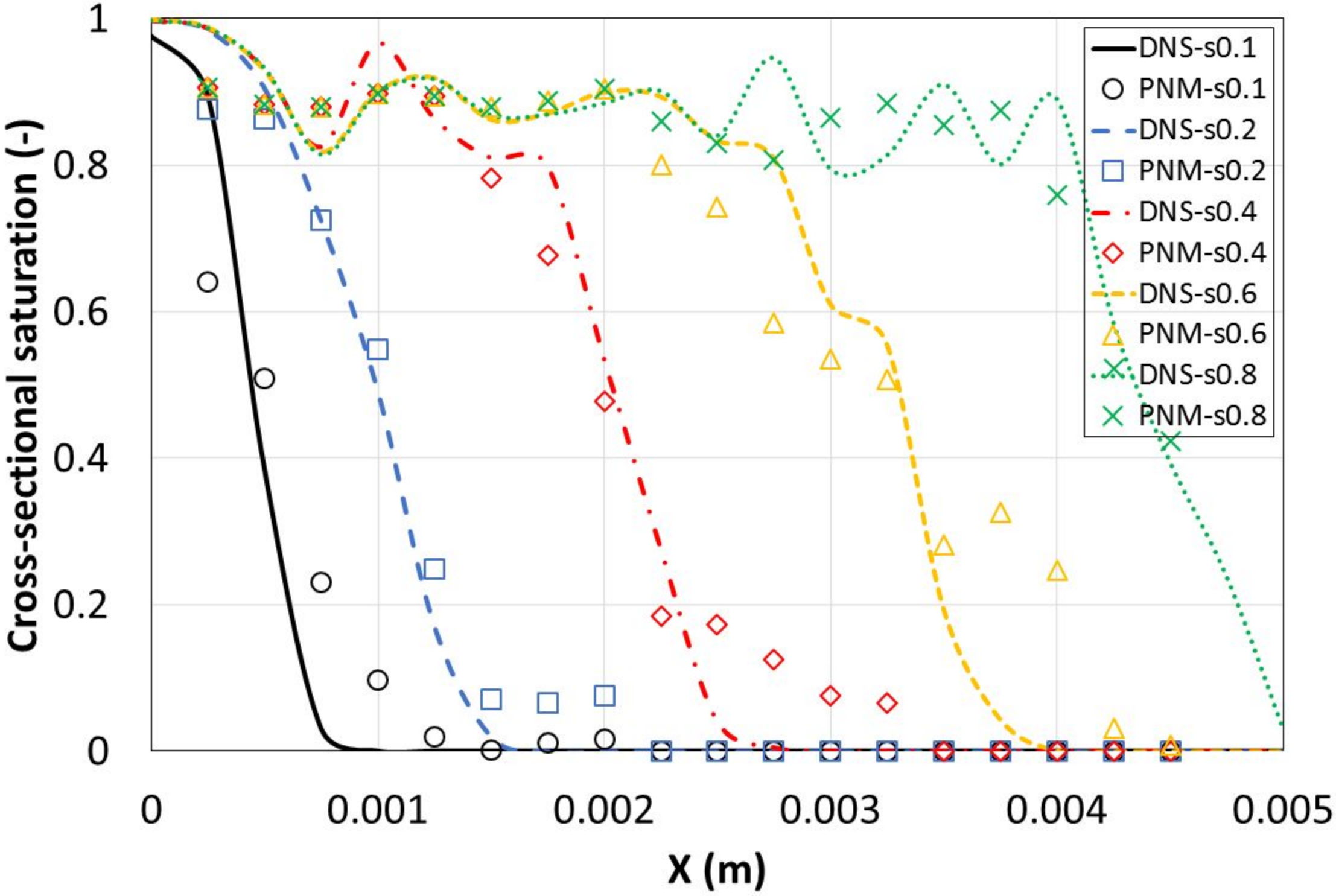
Cross-sectional saturation (-)
X (m)
0
0.2
0.4
0.6
0.8
1
0
0.001
0.002
0.003
0.004
0.005
DNS-s0.1
PNM-s0.1
DNS-s0.2
PNM-s0.2
DNS-s0.4
PNM-s0.4
DNS-s0.6
PNM-s0.6
DNS-s0.8
PNM-s0.8

Figure 10.

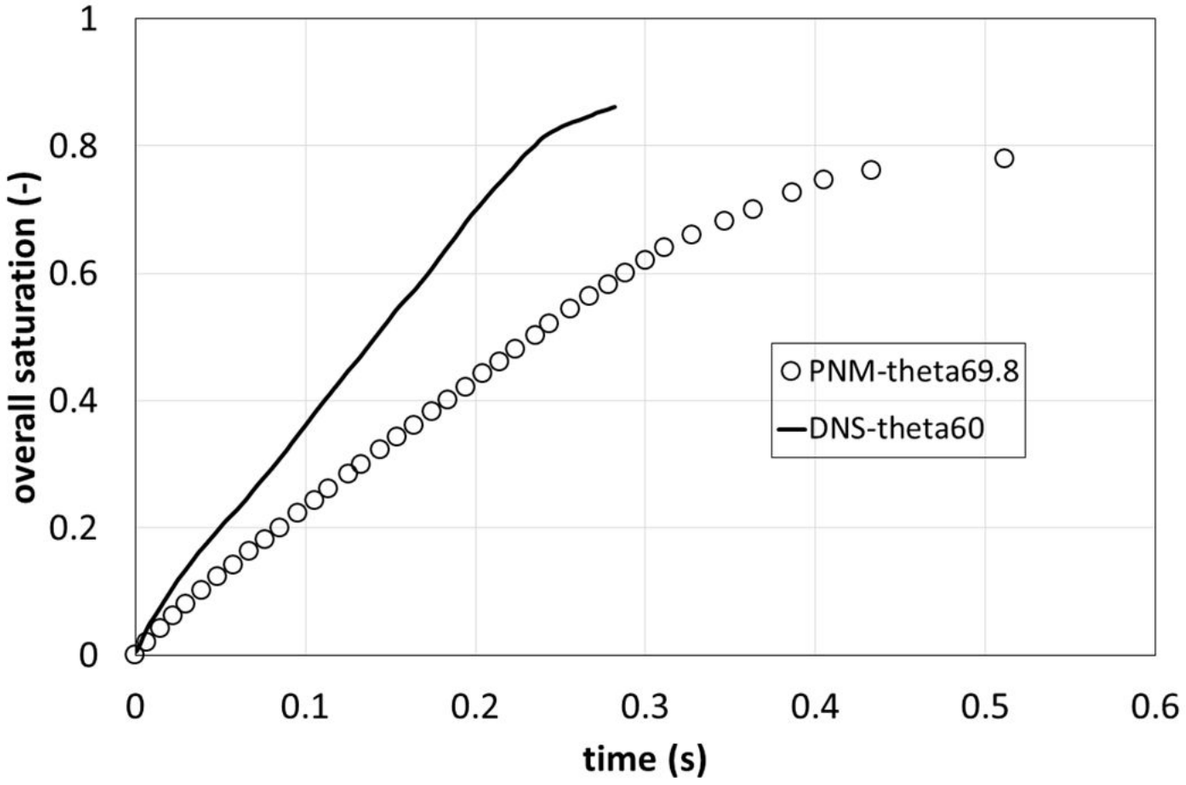
overall saturation (-)
time (s)
PNM-theta69.8
DNS-theta60
0
0.2
0.4
0.6
0.8
1
0
0.1
0.2
0.3
0.4
0.5
0.6

(a)

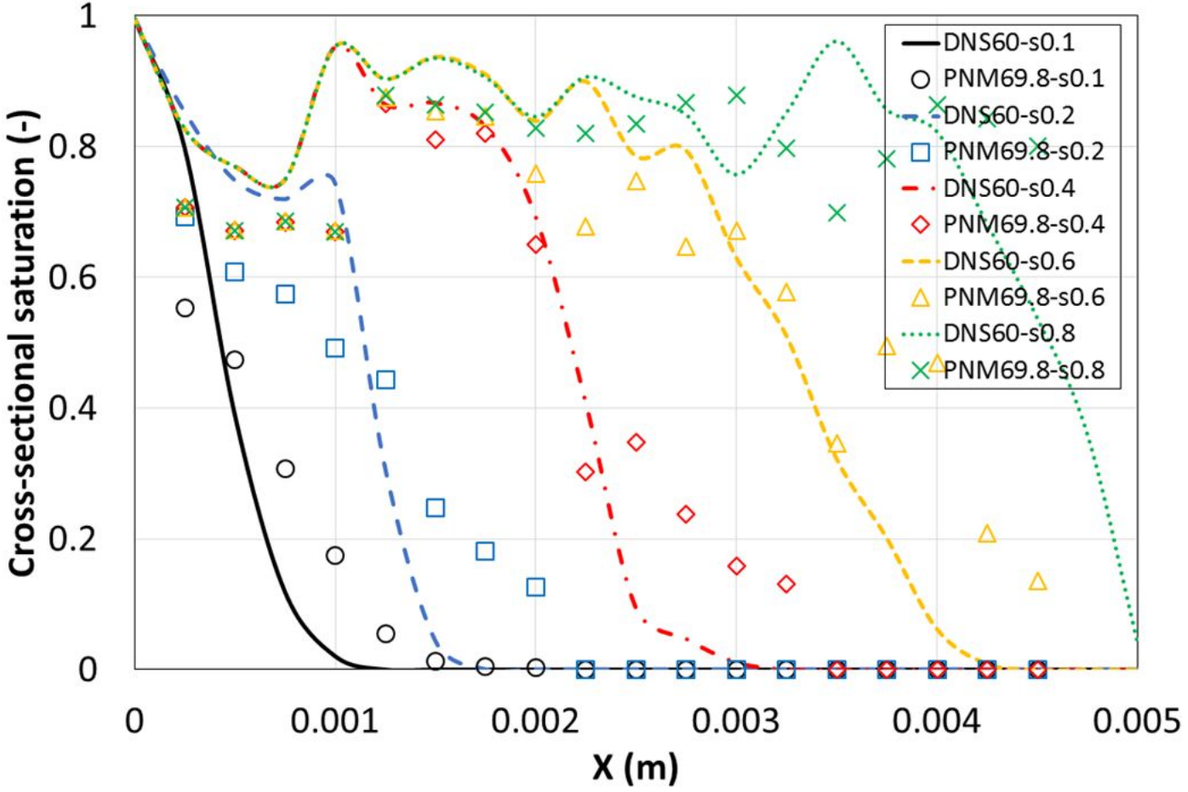
Cross-sectional saturation (-)
X (m)
DNS60-s0.1
PNM69.8-s0.1
DNS60-s0.2
PNM69.8-s0.2
DNS60-s0.4
PNM69.8-s0.4
DNS60-s0.6
PNM69.8-s0.6
DNS60-s0.8
PNM69.8-s0.8
0
0.2
0.4
0.6
0.8
1
0
0.001
0.002
0.003
0.004
0.005

(b)

Figure 11.

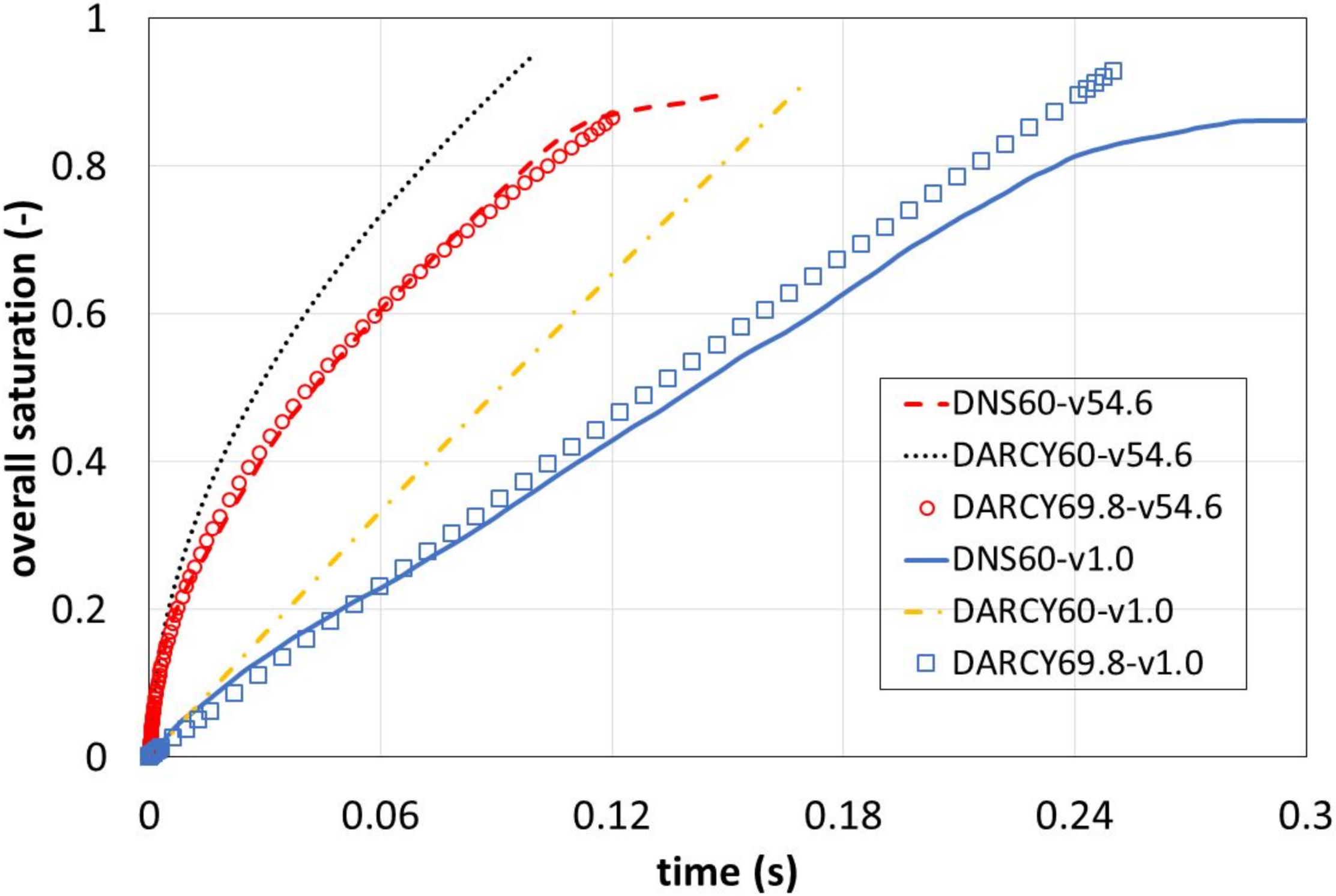
1
0.8
0.6
0.4
0.2
0
overall saturation (-)
0
0.06
0.12
0.18
0.24
0.3
time (s)
DNS60-v54.6
DARCY60-v54.6
DARCY69.8-v54.6
DNS60-v1.0
DARCY60-v1.0
DARCY69.8-v1.0

Figure 12.

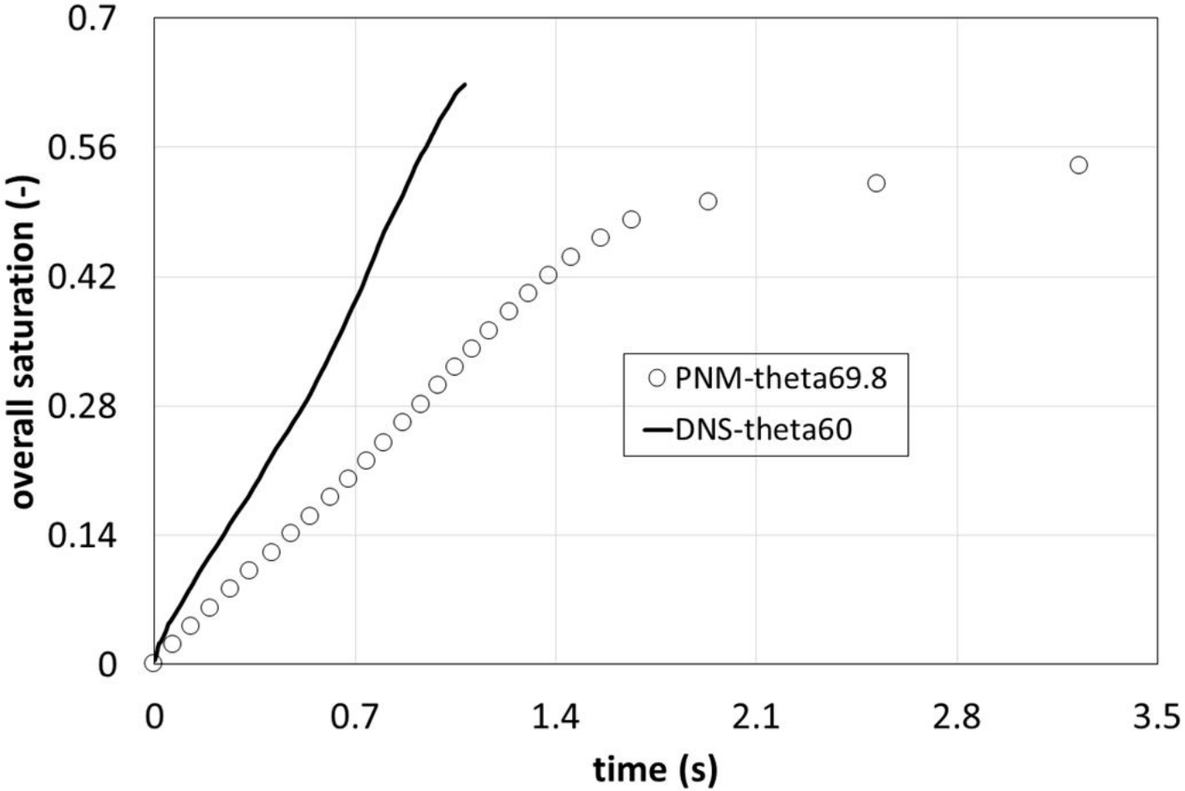
0.7
0.56
0.42
0.28
0.14
0
overall saturation (-)
0
0.7
1.4
2.1
2.8
3.5
time (s)
PNM-theta69.8
DNS-theta60

(a)

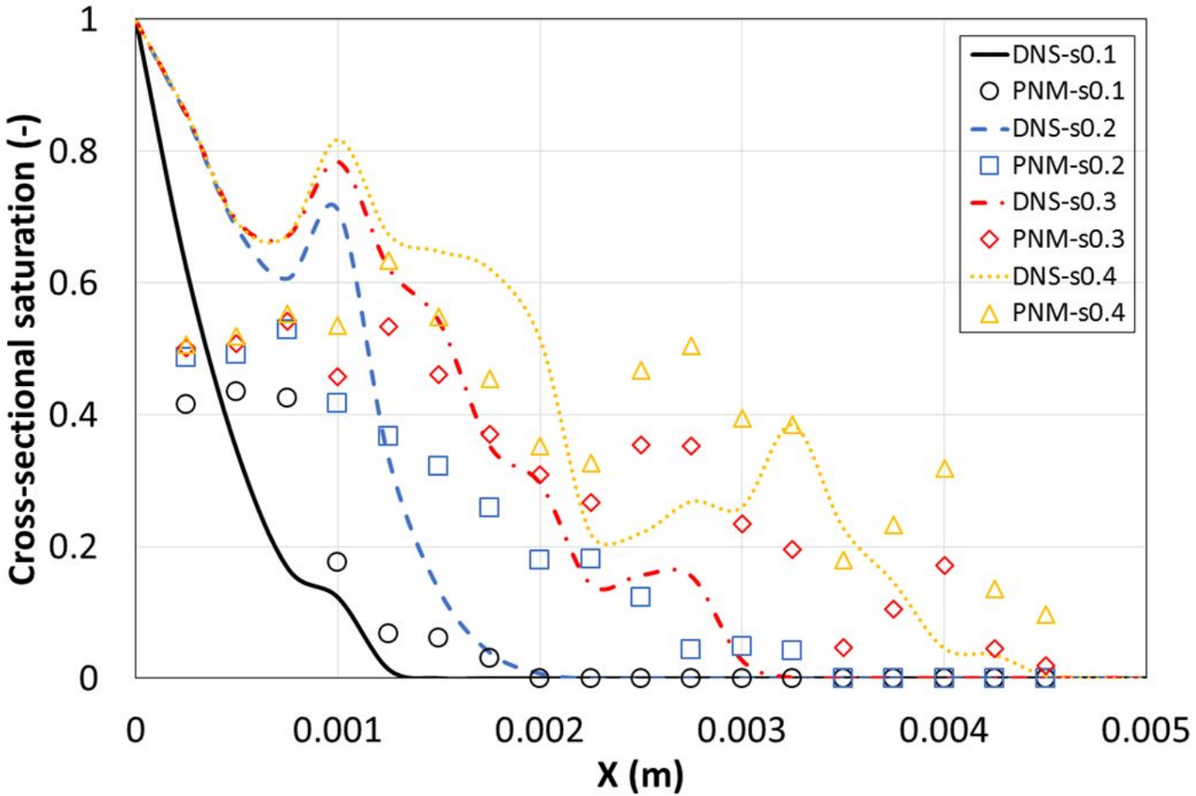
1
0.8
0.6
0.4
0.2
0
Cross-sectional saturation (-)
0
0.001
0.002
0.003
0.004
0.005
X (m)
DNS-s0.1
PNM-s0.1
DNS-s0.2
PNM-s0.2
DNS-s0.3
PNM-s0.3
DNS-s0.4
PNM-s0.4

(b)

Figure 13.

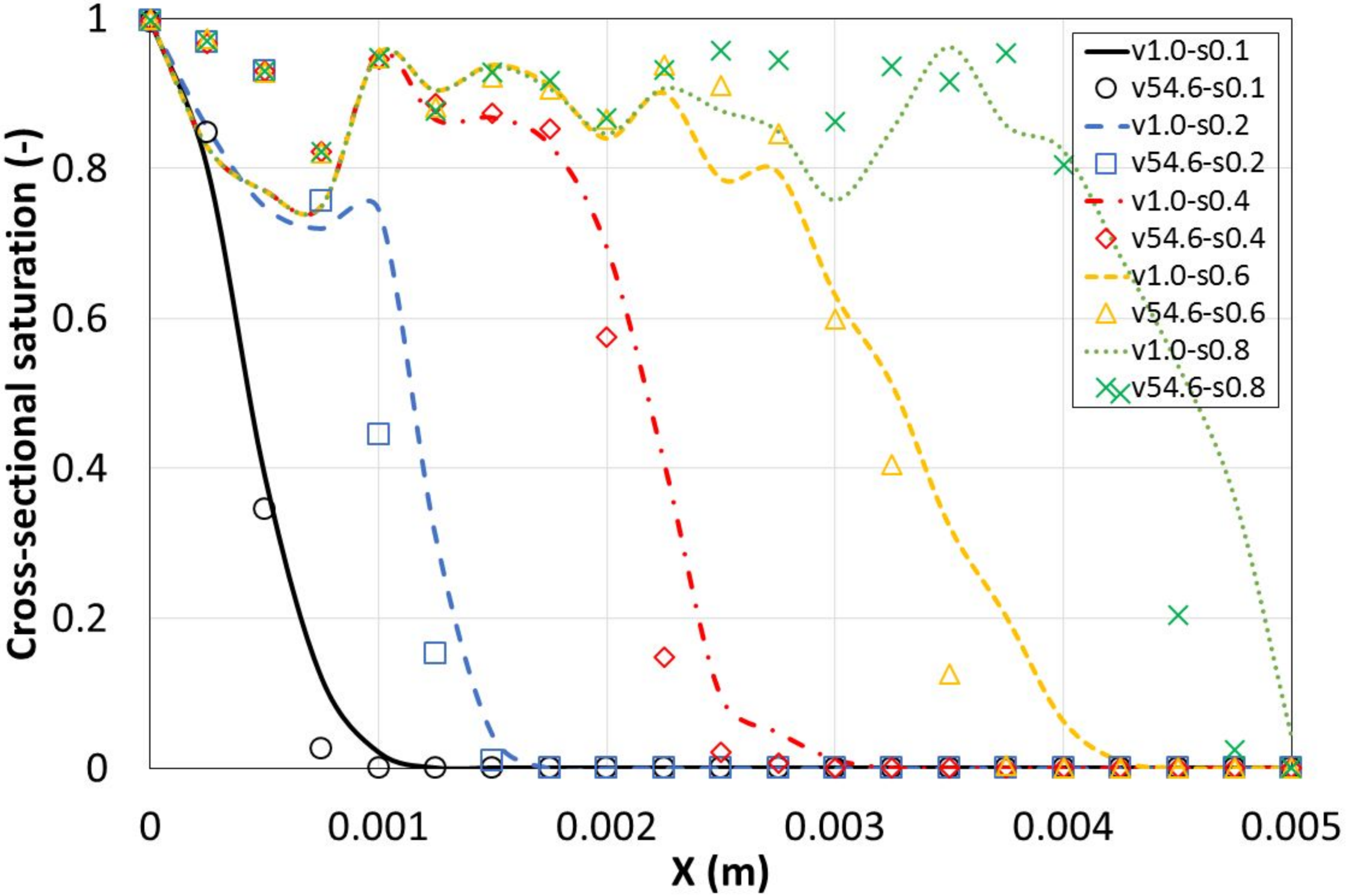
Cross-sectional saturation (-)
X (m)
0
0.2
0.4
0.6
0.8
1
0
0.001
0.002
0.003
0.004
0.005
v1.0-s0.1
v54.6-s0.1
v1.0-s0.2
v54.6-s0.2
v1.0-s0.4
v54.6-s0.4
v1.0-s0.6
v54.6-s0.6
v1.0-s0.8
v54.6-s0.8

Figure A1.

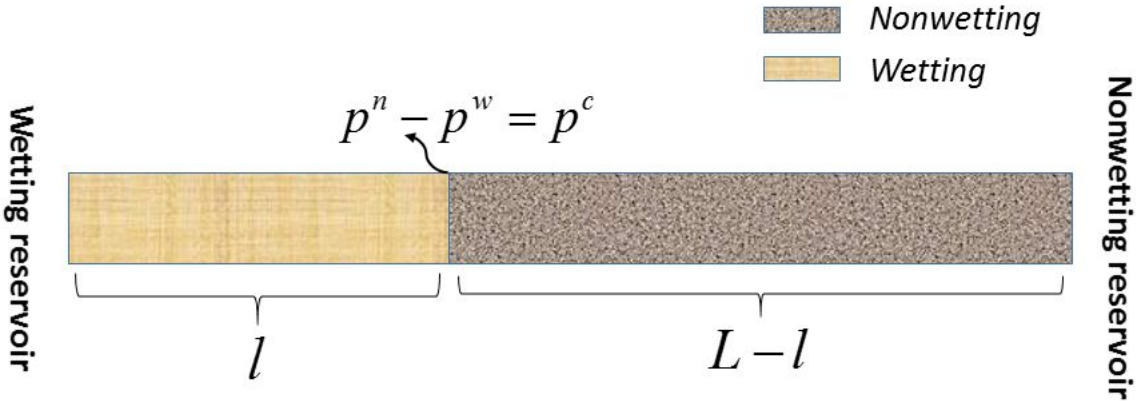
Nonwetting
Wetting
$p^n - p^w = p^c$
Wetting reservoir
Nonwetting reservoir
l
$L - l$

Figure B1.

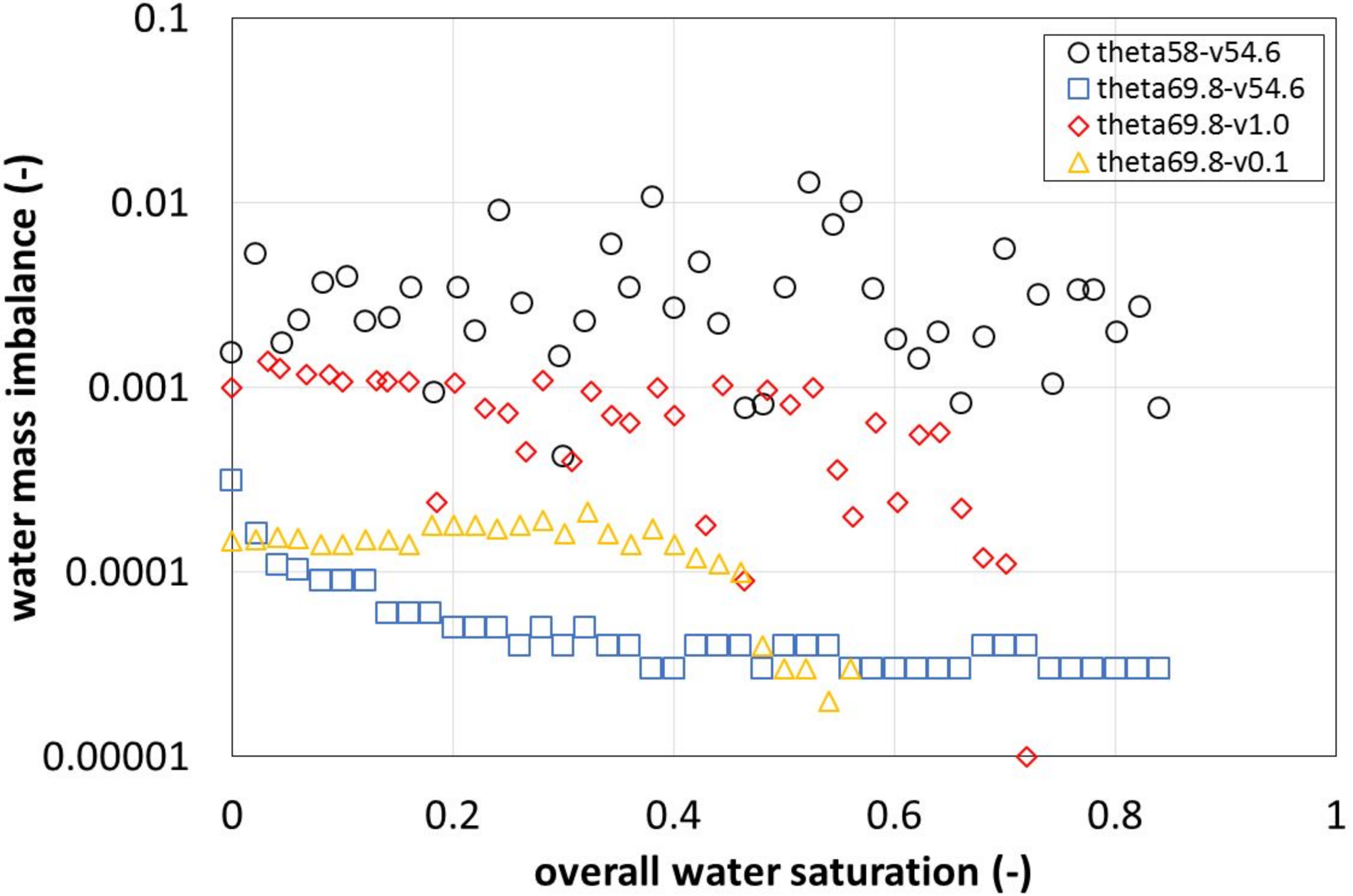
0.1
0.01
0.001
0.0001
0.00001
water mass imbalance (-)
0
0.2
0.4
0.6
0.8
1
overall water saturation (-)
theta58-v54.6
theta69.8-v54.6
theta69.8-v1.0
theta69.8-v0.1

Figure B2.

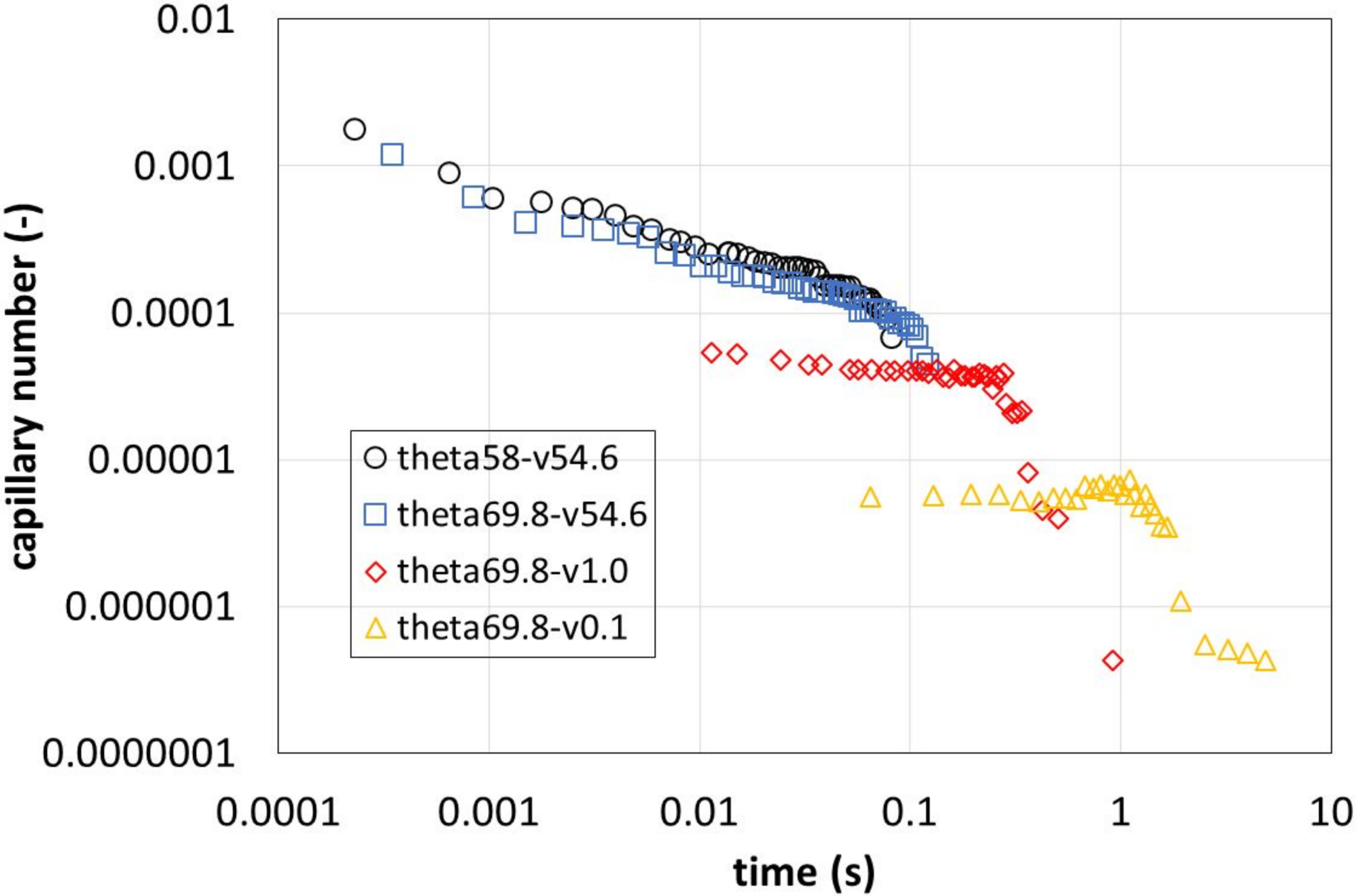
0.01
0.001
0.0001
0.00001
0.000001
0.0000001
capillary number (-)
0.0001
0.001
0.01
0.1
1
10
time (s)
theta58-v54.6
theta69.8-v54.6
theta69.8-v1.0
theta69.8-v0.1